



**HAL**  
open science

# Experimental Characterization of Cohesive Zone Models for Thin Adhesive Layers Loaded in Mode I, Mode II, and Mixed-Mode I/II by the use of a Direct Method

G. Lélías, Eric Paroissien, Frederic Lachaud, Joseph Morlier

## ► To cite this version:

G. Lélías, Eric Paroissien, Frederic Lachaud, Joseph Morlier. Experimental Characterization of Cohesive Zone Models for Thin Adhesive Layers Loaded in Mode I, Mode II, and Mixed-Mode I/II by the use of a Direct Method. *International Journal of Solids and Structures*, 2019, 10.1016/j.ijsolstr.2018.09.005 . hal-01878722

**HAL Id: hal-01878722**

**<https://hal.science/hal-01878722>**

Submitted on 21 Sep 2018

**HAL** is a multi-disciplinary open access archive for the deposit and dissemination of scientific research documents, whether they are published or not. The documents may come from teaching and research institutions in France or abroad, or from public or private research centers.

L'archive ouverte pluridisciplinaire **HAL**, est destinée au dépôt et à la diffusion de documents scientifiques de niveau recherche, publiés ou non, émanant des établissements d'enseignement et de recherche français ou étrangers, des laboratoires publics ou privés.

1 **Experimental Characterization of Cohesive Zone Models for Thin Adhesive Layers**  
2 **Loaded in Mode I, Mode II, and Mixed-Mode I/II by the use of a Direct Method**

3  
4  
5

6 G. Lélías<sup>1,2</sup>, E. Paroissien<sup>1,\*</sup>, F. Lachaud<sup>1</sup> and J. Morlier<sup>1</sup>

7  
8

9 <sup>1</sup> *Institut Clément Ader (ICA), Université de Toulouse, UPS, INSA, ISAE-SUPAERO, MINES-ALBI, CNRS, 3 rue*  
10 *Caroline Aigle, 31400 Toulouse, France*

11 <sup>2</sup> *SOGETI HIGH TECH, AEROPARK, 3 Chemin Laporte, 31300 Toulouse, France*

12  
13

14  
15

16  
17

18  
19

20  
21

22 \*To whom correspondence should be addressed: Tel. +33561338438, E-mail: [eric.paroissien@isae-supero.fr](mailto:eric.paroissien@isae-supero.fr)

23  
24

25  
26

27  
28

1  
2  
3  
4  
5  
6  
7  
8  
9  
10  
11  
12  
13  
14  
15  
16  
17  
18  
19  
20  
21  
22  
23  
24

**Abstract** – The demand for designing lightweight structures without any loss of strength or stiffness has conducted many engineers and researchers to seek for alternative joining methods. In this context, adhesive bonding may appear as an attractive joining method. However the interest of adhesive bonding remains while the structural integrity of the joint is ensured. According to recent literature the Cohesive Zone Model (CZM) appears as a suitable approach able to predict both static and fatigue strength of adhesively bonded joints. This approach of the fracture process of adhesive layers is based on the modeling of the adhesive mechanical behavior through a set of adhesive cohesive properties in either mode I, mode II or mixed-mode I/II. The strength prediction of adhesively bonded joints is then highly dependent on the CZM parameters. The methods used to experimentally characterize them are thus essential. A new methodology, termed direct method, is presented and tested. It is based on the measurement of displacement field of bonded adherends at the crack tip of classical specimens allowing for the loading of the adhesive layer in pure mode I, pure mode II and mixed-mode I/II. The tested adhesive is a methacrylate-based two-component adhesive paste found under the reference SAF30 MIB manufactured by AEC Polymers (ARKEMA group). The adherends are in aluminium 6060. It is shown that it is possible to characterize the cohesive properties of the adhesive layer using the direct method. The numerical tests involve both adherends and adhesive nonlinearities. Nevertheless, the presented experimental implementation passes by the development of a dedicated data pre-processing to interpret the experimental measurements, highlighting the significance of the choice of the measurement means linked to the design of specimen.

**Key words:** *adhesively bonded joint, cohesive zone model, macro-element, mode I, mode II, mixed-mode I/II, singular value decomposition, digital image correlation technique*

# 1 NOMENCALTURE AND UNITS

2	<i>BBe</i>	bonded-beams element
3	<i>CZM</i>	cohesive zone model
4	<i>DIC</i>	digital image correlation
5	<i>DoE</i>	design of experiments
6	<i>DCB</i>	double cantilever beam
7	<i>ENF</i>	end notched flexure
8	<i>FE</i>	Finite Element
9	<i>ME</i>	macro-element
10	<i>MMB</i>	mixed mode bending
11	<i>OSRA</i>	optimal sub rank approximation
12	<i>SLJ</i>	single-lap joint
13	<i>SVD</i>	singular value decomposition
14	$A_j$	extensional stiffness (N) of adherend $j$
15	$B_j$	extensional and bending coupling stiffness (N.mm) of adherend $j$
16	$D_j$	bending stiffness (N.mm <sup>2</sup> ) of adherend $j$
17	$E$	adherend Young's modulus (MPa)
18	$G_I$	strain energy release rate (energy per unit of area: mJ or N/mm) in peel
19	$G_{II}$	strain energy release rate (energy per unit of area: mJ or N/mm)in shear
20	$G_{Ic}$	critical strain energy release rate (energy per unit of area: mJ or N/mm)in peel
21	$G_{Ie}$	adhesive elastic strain energy stored (energy per unit of area: mJ or N/mm)in peel
22	$G_{IIc}$	critical strain energy release rate (energy per unit of area: mJ or N/mm)in shear
23	$G_{IIe}$	adhesive elastic strain energy stored (energy per unit of area: mJ or N/mm)in shear
24	$H$	magnitude of applied displacement (mm)
25	$J$	J-integral parameter
26	$K_{BBe}$	elementary stiffness matrix of a bonded-beam element
27	$L$	length (mm) of bonded overlap
28	$M_j$	bending moment (N.mm) in adherend $j$ around the $z$ direction
29	$N_j$	normal force (N) in adherend $j$ in the $x$ direction
30	$P$	magnitude of applied force (N)

1	$S$	adhesive peel stress (MPa)
2	$S_{max}$	maximal adhesive peel stress (MPa)
3	$T$	adhesive shear stress (MPa)
4	$T_{max}$	maximal adhesive shear stress (MPa)
5	$V_j$	shear force (N) in adherend $j$ in the $y$ direction
6	$a$	crack length (mm)
7	$b$	width (mm) of the adherends
8	$d$	damage parameter
9	$e$	thickness (mm) of the adhesive layer
10	$h_j$	half thickness (mm) of adherend $j$
11	$k_I$	adhesive elastic stiffness (MPa/mm) in peel
12	$k_{II}$	adhesive elastic stiffness (MPa/mm) in shear
13	$n$	power used in the adhesive material law
14	$n_{ME}$	number of macro-elements
15	$t$	adherend thickness (mm)
16	$u_j$	displacement (mm) of adherend $j$ in the $x$ direction
17	$v_j$	displacement (mm) of adherend $j$ in the $y$ direction
18	$\Delta$	overlap length (mm) of a macro-element
19	$\Delta_j$	characteristic parameter of adherend $j$ in $N^2 \cdot mm^2$
20	$\alpha$	angle (rad) used for the definition the load application in MCB test
21	$\beta$	mixed-mode parameter
22	$\delta_t$	numerical time step (s)
23	$\delta_u$	displacement jump (mm) of the interface along the $x$ -axis
24	$\delta_{ue}$	displacement jump (mm) of the interface along the $x$ -axis at initiation
25	$\delta_{uf}$	displacement jump (mm) of the interface along the $x$ -axis at propagation
26	$\delta_v$	displacement jump (mm) of the interface along the $y$ -axis
27	$\delta_{ve}$	displacement jump (mm) of the interface along the $x$ -axis at initiation
28	$\delta_{vf}$	displacement jump (mm) of the interface along the $x$ -axis at propagation
29	$\lambda$	norm of displacement jump (mm) of the interface
30	$\lambda_e$	norm of displacement jump (mm) of the interface at initiation

1  $\lambda_f$  norm of displacement jump (mm) of the interface at propagation

2  $\nu$  adherend Poisson's ratio

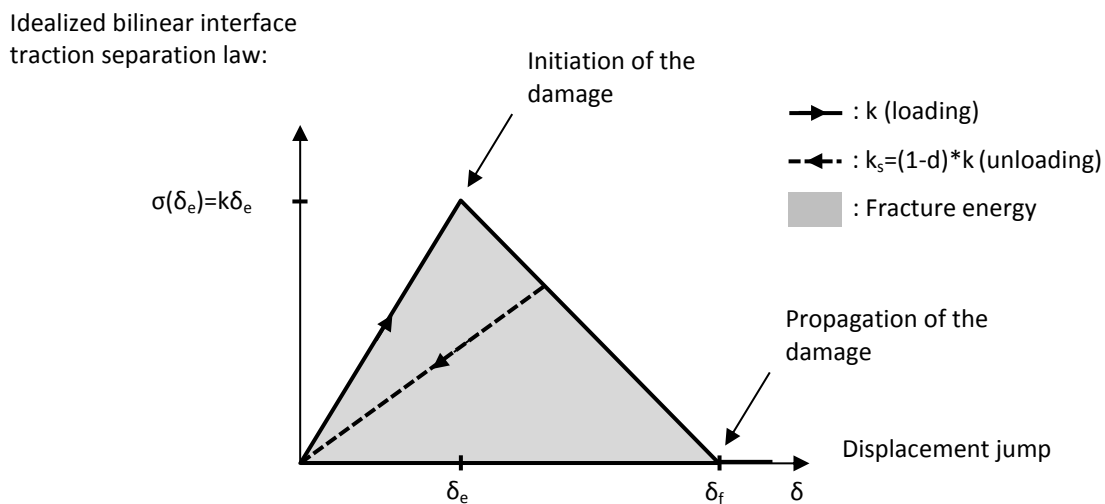
3  $\theta_j$  bending angle (rad) of the adherend  $j$  around the  $z$  direction

4

## 5 **1. Introduction**

6 In the frame of structural design, the choice of joining technologies is decisive since they guarantee the integrity  
7 of the manufactured system. The mechanical fastening, such as riveting or screwing, appears the reliable solution  
8 for the designers. Nevertheless alone or in combination with the mechanical fastening, the adhesive bonding  
9 joining technology may offer significantly improved mechanical performance in terms of stiffness, static  
10 strength and fatigue strength (Hart-Smith 1980, Kelly 2006). The use of this higher level of mechanical  
11 performance allows for the design of lighter joints. In other words, the adhesive bonding offers the possibility to  
12 reduce the structural mass while ensuring the mechanical strength. The optimization of the strength-to-mass ratio  
13 is a challenge for several industrial sectors, such as aerospace, automotive, rail or naval transport industries. But,  
14 the reduction of structural mass makes sense only if the structural integrity is ensured. As result to take benefit  
15 from the adhesive bonding in view of mass reduction, it is required to be able to predict the strength of bonded  
16 joints. The strength prediction consists in the comparison of computed strength criteria to design allowable  
17 value. The strength criteria could be based on theoretical, empirical, semi-empirical investigations and possibly  
18 including in-service feedback. The stress analysis allows for the computation of input data, mandatory to the  
19 assessment of strength criteria. The experimental characterization allows then for the definition of design  
20 allowable value as well as of mechanical behavior to be used as input data of the mechanical analysis. As  
21 highlighted in (Jumel *et al.* 2013), the strength of a same joining system at macroscale depends on the  
22 experimental test specimen and procedure used, which contributes in restricted reliability or in extensive and  
23 expensive experimental test campaign. According to (Li *et al.* 2006, Khoramishad *et al.* 2010, Khoramishad *et al.*  
24 *et al.* 2011, Da Silva and Campilho 2012), the cohesive zone modeling – denoted CZM – appears as one of the  
25 most suitable approach able to model both the static and the fatigue behavior of adhesive joints. According to  
26 (Khoramishad *et al.* 2010), the CZM have the advantage of: (i) considering finite strains and stresses at the  
27 adhesive crack tip, (ii) indicating both damage initiation and propagation as direct outputs of the model, (iii)  
28 advancing the crack tip as soon as the local energy release rate reaches its critical value with no need of complex  
29 moving mesh techniques. Based on Continuum Damage Mechanics and Fracture Mechanics, the CZM enables a  
30 diagnostic of the current state of the adhesive interface damage along the overlap. The damage, associated to

1 micro-cracks and/or voids coalescence, results in a progressive degradation of the material stiffness before  
 2 failure. An idealization of a CZM bilinear stress-strain relationship or CZM bilinear traction separation law is  
 3 presented in Figure 1. The CZM bilinear traction separation law is a well-established interface behavior that first  
 4 assumes a linearly dependency relationship between the interface separation (deformation) and the resulting  
 5 traction (stress). Once a prescribed value of separation is reached by the adhesive, the damage initiation is  
 6 described in the form of a linearly decreasing resulting traction. Finally, the propagation of the damage is  
 7 described by voluntarily fixing the resulting traction to zero, hence modeling the creation of two traction-free  
 8 surfaces (i.e.: physical cracking). Both damage initiation and damage propagation phases are addressed in the  
 9 model with no need of assuming any initial crack in the material (Valoroso and Champaney 2004, De Moura *et*  
 10 *al.* 2009, Campilho *et al.* 2013).



11  
 12 **Figure 1.** Representation for an idealized bilinear interface traction separation law.

13  
 14 The strength prediction of adhesively bonded joints is then highly dependent on the CZM parameters. The  
 15 methods used to experimentally characterize them are thus essential. As a result, numbers of authors have  
 16 addressed this critical point over the past few years (Anderson and Stigh 2004, Alfredsson *et al.* 2003,  
 17 Alfredsson 2004, Leffler *et al.* 2006, Högberg 2006, Högberg and Stigh 2006, Cui *et al.* 2014, Azari *et al.* 2009,  
 18 Gowrishankar S. *et al.* 2012, Wu *et al.* 2016). Most of these methods make use of the concept of the energetical  
 19 balance associated to the computation of the path independent J-integral (Rice 1968) along a closed contour of  
 20 specifically designed joint specimens, known as the inverse method (Anderson and Stigh 2004, Alfredsson *et al.*  
 21 2003, Alfredsson 2004, Leffler *et al.* 2006, Högberg 2006, Högberg and Stigh 2006). The inverse method is

1 based on the energetical balance associated with the computation of the path independent J-integral (Rice 1968)  
2 on a closed contour  $\Gamma$ :

$$3 \quad J = \int W dy - \bar{T} \frac{d\bar{U}}{dx} ds \quad (1)$$

4 where  $W$  refers to the strain energy density,  $\bar{T} = n\sigma$  to the traction vector,  $\sigma$  to the stress tensor,  $\bar{U}$  to the  
5 displacement vector,  $n$  to the normal unit vector directed outward to the counter-clock wise integration path  $\Gamma$ ,  
6 and  $(x,y)$  to the specified two-dimensional coordinate system. From the fundamental work by (Fraisie and  
7 Schmit 1993) it is shown that the J-integral parameter can be computed from stress analysis based on a model of  
8 beam on an elastic foundation as:

$$9 \quad J(\delta_u, \delta_v) = \int_0^{\delta_u} T(\delta_u, \delta_v) d\delta_u + \int_0^{\delta_v} S(\delta_u, \delta_v) d\delta_v \quad (2)$$

10 In the frame of the inverse method:

11 (i) the adhesive peel stress is obtained from experimental tests under pure mode I loading as (Anderson and Stigh  
12 2004):

$$13 \quad S(\delta_v) = \frac{\partial J(\delta_u, \delta_v)}{\partial \delta_v} \quad (3)$$

14 (ii) the adhesive shear stress is obtained from experimental tests under pure mode II loading as (Alfredsson *et al.*  
15 2003):

$$16 \quad T(\delta_u) = \frac{\partial J(\delta_u, \delta_v)}{\partial \delta_u} \quad (4)$$

17 (iii) the adhesive peel and shear stresses are obtained from experimental tests under mixed-mode I/II loading as  
18 (Högberg 2006, Högberg and Stigh 2006):

$$19 \quad S(\delta_v) = \frac{\partial J(\delta_u, \delta_v)}{\partial \delta_v} \quad (5)$$

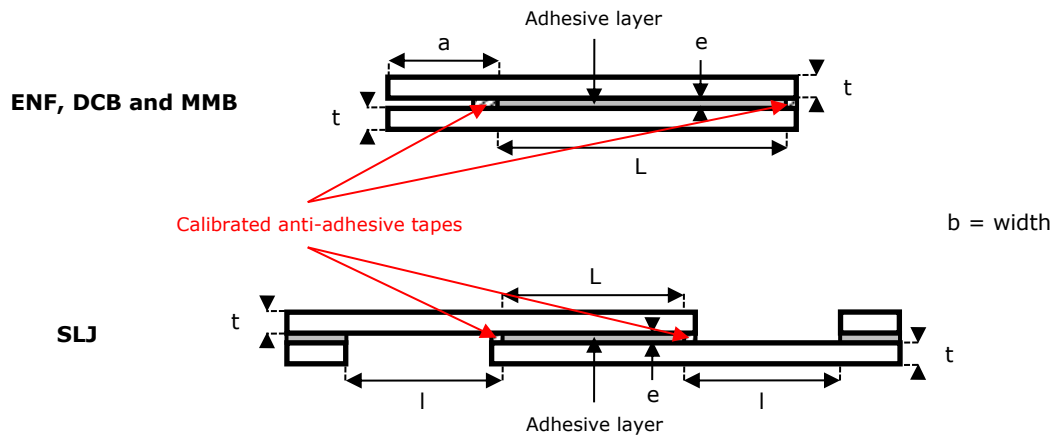
$$20 \quad T(\delta_u) = \frac{\partial J(\delta_u, \delta_v)}{\partial \delta_u} \quad (6)$$

21 The adhesive stresses are then derived from the J-integral. An advantage of this method is that it offers the  
22 possibility to monitor the evolution of the adhesive stress at the crack tip from the measurement of macroscopic  
23 quantities possibly measurable from experimental test fixtures, such as the applied load (in N) or the evolution of  
24 displacement jump (in mm) at the crack tip. Numbers of joint specimens have been explored for pure mode I,  
25 pure mode II and mixed-mode I/II characterization of adhesive layers. According to (Da Silva and Campilho  
26 2012), end notched flexure (ENF) and double cantilever beam (DCB) joint specimens have respectively emerged  
27 as the joint specimens the most frequently used for characterizing the cohesive properties of thin adhesive  
28 interfaces in pure mode I and pure mode II over the past years. An idealization of the linear elastic distributions



1 is path-independent along the spatial integration path, it is shown that the J-integral, which is shown to be a  
 2 potential function from which derive the cohesive stress, is dependent on the loading path history. A direct  
 3 consequence for truss-like CZMs is thus that Eq. (2) does not imply Eq. (5) and Eq. (6), so that the use of the  
 4 inverse method should not be suitable to any type of CZM.

5 The objective of this paper is to suggest a direct method to assess CZMs for the modelling of adhesively bonded  
 6 joints, overcoming the restrictions involved in methods based on J-integral. In the first part, the inverse method  
 7 is employed on the results of a numerical test campaigns on MCB configuration. A mixed-mode CZM based on  
 8 the definition of pure mode bilinear laws linked by interaction laws under mixed-mode is used for this test  
 9 campaign in order to show the deviation of predictions obtained from the inverse method. The numerical  
 10 analyses are performed using three-dimensional Finite Element (3D FE) model as well as the macro-element  
 11 (ME) technique (Paroissien 2006a, Paroissien *et al.* 2006b, Paroissien *et al.* 2007, Paroissien *et al.* 2013, Lélías  
 12 *et al.* 2015). In the second part, an approach based on design of experiments (DoE) is presented to assess the  
 13 main parameters affecting the experimental assessment of CZM. Finally, in the part, the direct method is applied  
 14 to characterize the CZM properties in mode I, mode II and mixed-mode I/II through the use of double cantilever  
 15 beam (DCB) specimen, end notched flexure (ENF) specimen and mixed mode bending (MMB) specimen,  
 16 respectively (see Figure 3). Finally the single-lap bonded joint (SLJ) configuration is used to assess the relevance  
 17 of the method (see Figure 3).



18  
 19 **Figure 3.** Schematic representation for the manufacturing process of the ENF, DCB, MMB and SLJ joint  
 20 specimens.

21

## 22 2. Numerical test campaign

### 23 2.1. Overview of the numerical test campaign

1 In the frame of the numerical test campaign presented in this paper, the MCB test configuration has been  
 2 selected. It has been suggested by Högberg and Stigh (Högberg and Stigh 2006). Similarly to the DCB test  
 3 configuration, the loading consists in a pair of forces (termed  $P$ ), being of the same magnitude but in opposite  
 4 directions. Nevertheless, the action direction of the pair of forces is defined by an angle  $\alpha$ , which allows for the  
 5 adhesive layer to be submitted to pure mode I, pure mode II and mixed-mode I/II (see Figure 2). The selected  
 6 specimen design, including geometrical and material parameters, corresponds to the one described by Högberg  
 7 and Stigh (Högberg and Stigh 2006). The crack length  $a=0$  is then chosen. The geometrical parameters are  
 8 provided in Table 1 in conjunction with Figure 2. In this numerical test campaign, only one angle  $\alpha$  is chosen  
 9  $\alpha=\pi/16$ .

11 Table 1. Geometrical parameters of the MCB specimen.

a in mm	b in mm	e in mm	t in mm	L in mm
0	4	0.2	8	100

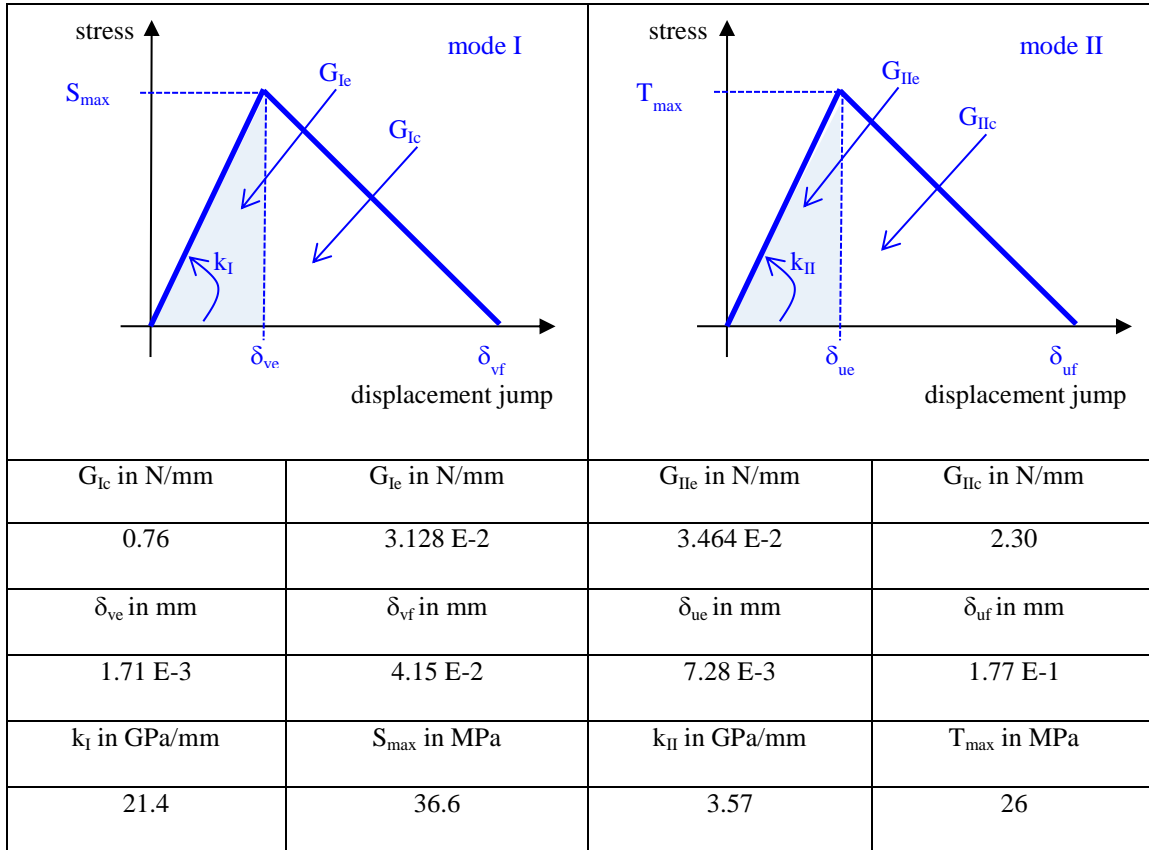
12  
 13 The adherends are made of steel with a Young's modulus  $E=200\text{ GPa}$  and a Poisson's ratio  $\nu=0.3$ . The design is  
 14 such that the adherends will remain in their linear elastic domain. The adhesive is assumed to have a classical  
 15 bilinear damage evolution law following (Allix and Ladevèze 1996), involving interaction energy laws for both  
 16 initiation and propagation under mixed-mode:

$$17 \begin{cases} \left(\frac{G_I}{G_{Ie}}\right)^n + \left(\frac{G_{II}}{G_{IIe}}\right)^n = 1 \\ \left(\frac{G_I}{G_{Ic}}\right)^m + \left(\frac{G_{II}}{G_{IIc}}\right)^m = 1 \end{cases} \quad (7)$$

18 where  $n=m$  is a material parameter to be identified,  $G_{Ic}$  and  $G_{IIc}$  are the critical strain energy release rate in mode  
 19 I and mode II,  $G_{Ie}$  and  $G_{IIe}$  are the elastic strain energies stored in mode I and mode II and  $G_I$  and  $G_{II}$  are related  
 20 to the strain energy release rates in mode I and mode II, respectively. For this numerical test campaign,  $n=1$  is  
 21 chosen. The fracture energies in mode I and mode II and the elastic stiffnesses under peel and shear, termed  $k_I$   
 22 and  $k_{II}$  respectively are the same as those used by Högberg and Stigh (Högberg and Stigh 2006). Nevertheless,  
 23 the adhesive maximal peel and shear stresses, termed  $S_{max}$  and  $T_{max}$ , is different, to ensure a right energy  
 24 dissipation during loading (Turon et al. 2010). It is indicated that the law by Allix and Ladevèze (Allix and  
 25 Ladevèze 1996) already includes this condition. It is then chosen to keep the same maximal shear stress  $T_{max}=26$   
 26  $\text{MPa}$ , resulting in a maximal peel stress  $S_{max}=36.6\text{ MPa}$ , instead of  $20\text{ MPa}$ . The choice consisting in keeping  
 27  $S_{max}$  to its original value instead of  $T_{max}$  does not change qualitatively the results provided in his paper. The

1 material parameters of the adhesive layer are given in Table 2. In the following, the 3D FE model and the ME  
 2 model are presented. Then the results of the numerical test campaign are provided including those relating to the  
 3 convergence study of numerical models. Finally, the direct method is described.

4  
 5 Table 2. Adhesive material parameters.



6

7 2.2. Macro-element model

8 **Macro-element technique.** The numerical analysis is performed using the ME technique for the modelling of  
 9 bonded overlap (Paroissien 2006a, Paroissien *et al.* 2006b, Paroissien *et al.* 2007, Paroissien *et al.* 2013, Lélías *et*  
 10 *al.* 2015). The ME technique is inspired by the FE method and differs in the sense that the interpolation functions  
 11 are not assumed, since they take the shape of the solutions of the governing differential equation system. A direct  
 12 consequence is that only one ME is sufficient to mesh a complete bonded overlap in the frame of a linear stress  
 13 analysis. The bonded overlap is then modelled by a four-node ME – also called bonded-beams element – the  
 14 nodes of which are located at the extremities of the overlap on the neutral axes of adherends (see Figure 4). This  
 15 ME involves 3 degrees of freedom per node or a total of twelve for a 1D-beam analysis.

16

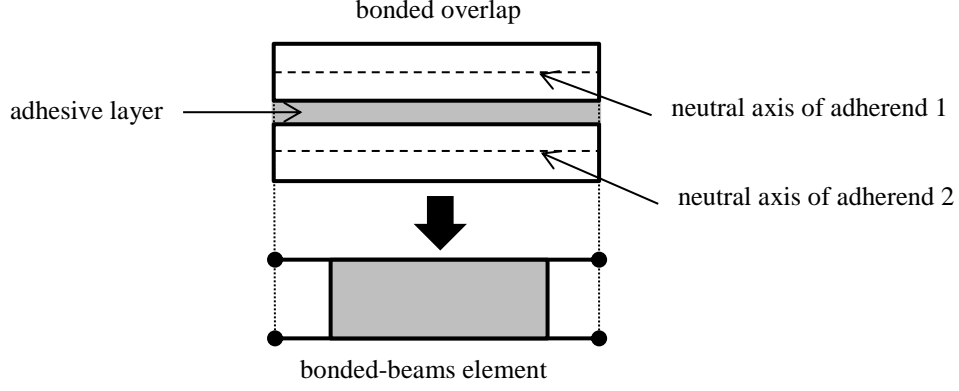


Figure 4. Modelling of a bonded overlap by a bonded-beams element.

1

2

3

4 The main work is thus the formulation of the elementary stiffness matrix of the bonded-beams element. Indeed

5 once the stiffness matrix of the complete structure is assembled from the elementary matrices and the boundary

6 conditions are applied, the minimization of the potential energy provides the solution, in terms of distributions

7 along the overlap of adhesives stresses, internal forces and displacements in the adherends. An approach for the

8 formulation of the stiffness has already been described in detail in previous papers (Paroissien 2006a, Paroissien

9 *et al.* 2006b, Paroissien *et al.* 2007, Paroissien *et al.* 2013, Lélías *et al.* 2015). Nevertheless, this approach could

10 be long to set up. In this paper, a new approach is provided in Appendix A for a fast and easy implementation

11 within a mathematical software such as SCILAB for example. Compared with the early approach, the shape of

12 solutions in terms of displacements and internal loads is not provided. Nevertheless, in the frame of nonlinear

13 material analyses such as the one presented in this paper, the bonded overlap has to be meshed in order to locally

14 update the material parameters within an iterative computation procedure. As a result, the displacements and

15 internal loads are directly read at nodes. Moreover, the following description is useful for the derivation of the

16 direct method.

17 **Hypotheses.** It is assumed that the thickness of the adhesive is constant along the length  $\Delta$  of the macro-element.

18 Moreover, the adherends are simulated as linear elastic Euler-Bernoulli laminated beams. The general shape of

19 the constitutive equations for the adherend  $j=1,2$  provides the six first differential equations:

$$20 \begin{cases} N_j = A_j \frac{du_j}{dx} - B_j \frac{d\theta_j}{dx} \\ M_j = -B_j \frac{du_j}{dx} + D_j \frac{d\theta_j}{dx} \\ \theta_j = \frac{dv_j}{dx} \end{cases} \Leftrightarrow \begin{cases} \frac{du_j}{dx} = \frac{D_j}{\Delta_j} N_j + \frac{B_j}{\Delta_j} M_j \\ \frac{dv_j}{dx} = \theta_j \\ \frac{d\theta_j}{dx} = \frac{B_j}{\Delta_j} N_j + \frac{A_j}{\Delta_j} M_j \end{cases} \quad (8)$$

1 where  $N_j (M_j)$  is the normal force (bending moment) of the adherend  $j$  and  $u_j (v_j, \theta_j)$  is the longitudinal  
 2 displacement (deflection, bending angle) of the adherend  $j$ . For the adherend  $j$ ,  $A_j$  represents the extensional  
 3 stiffness,  $D_j$  the bending stiffness and  $B_j$  the coupling stiffness and  $\Delta_j=A_jD_j-B_jB_j\neq 0$  (see Appendix C).

4 The adhesive layer is simulated by an infinite number of elastic shear and transverse springs attached at both  
 5 adherend interfaces. The adhesive shear stress – denoted  $T$  – and the adhesive peeling stress – denoted  $S$  – are  
 6 then given by:

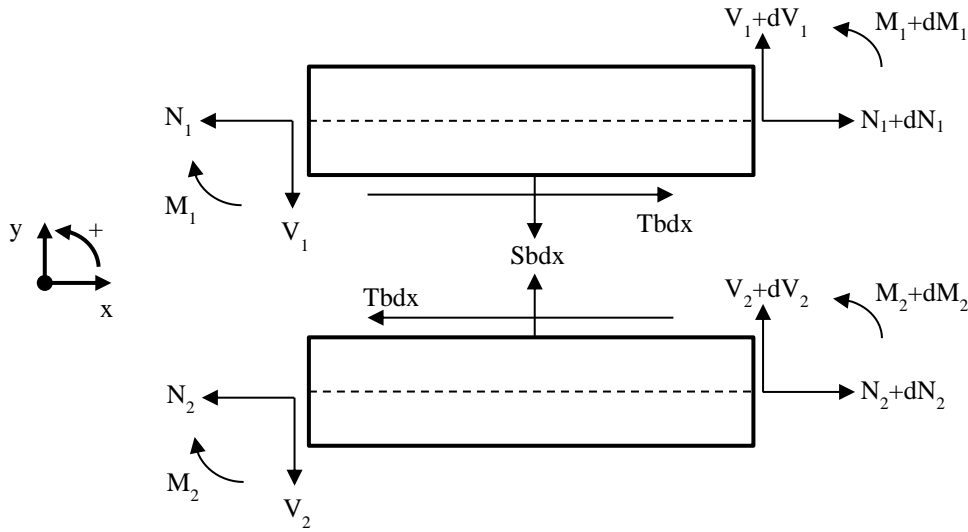
$$7 \quad \begin{cases} S = k_I(v_1 - v_2) \\ T = k_{II}(u_2 - u_1 - h_2\theta_2 - h_1\theta_1) \end{cases} \quad (9)$$

8 where  $h_j$  is the half thickness of adherend  $j$ . In this paper,  $h_1=h_2=t/2$ .

9 The classical local equilibrium from Goland and Reissner (Goland and Reissner 1944) is used and provides the  
 10 six last differential equations for  $j=1,2$  (see Figure 5):

$$11 \quad \begin{cases} \frac{dN_j}{dx} = (-1)^j bT \\ \frac{dV_j}{dx} = (-1)^{j+1} bS \\ \frac{dM_j}{dx} + V_j + bh_jT = 0 \end{cases} \quad (10)$$

12 where  $V_j$  is the shear force of the adherend  $j$ .



13  
 14 **Figure 5.** Free body diagram of infinitesimal elements of the adherend 1 (top) and adherend (bottom)

15  
 16 **Non linear computation.** The use of a nonlinear adhesive material implies that the computation is nonlinear. A  
 17 detailed description of the nonlinear algorithm used is provided in (Lélias *et al.* 2015). Only a brief overview is  
 18 given here. The algorithm is based on Newton-Raphson and uses the secant stiffness matrix with an update at

1 each iteration. In particular, the damage parameter is computed at each nodal abscissa according to the  
 2 introduced adhesive material law. The norm of displacement jump (in mm) of interface  $\lambda$  is defined by:

$$3 \quad \lambda = \sqrt{(\delta_v)^2 + (\delta_u)^2} \quad (11)$$

4 where  $\delta_v$  ( $\delta_u$ ) is the displacement jump of the interface (see Table 2) along the y-axis (x-axis). A mixity  
 5 parameter  $\beta$  is defined by:

$$6 \quad \beta = \frac{\delta_u}{\delta_v} = \frac{u_2 - u_1 - h_2 \theta_2 - h_1 \theta_1}{v_1 - v_2} \quad (12)$$

7 At each iteration, the mixity parameter  $\beta$  is updated. Under the current local mixity parameter, it assumed that  
 8 the material law is bilinear, so that the damage parameter  $d$  is such that:

$$9 \quad d = \frac{\lambda_f(\lambda - \lambda_e)}{\lambda(\lambda_f - \lambda_e)} \quad (13)$$

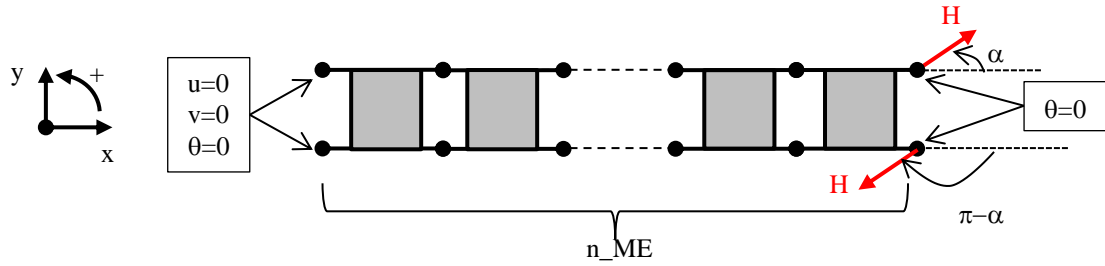
10 where  $\lambda_e$  ( $\lambda_f$ ) is the displacement jump (in mm) of the interface at initiation (propagation). In order to compute  $\lambda_e$   
 11 ( $\lambda_f$ ), the interaction laws Eq. (1) are used while classically assuming that the projections on pure modes of the  
 12 mixed mode evolution law under the current local mixity are bilinear (see Table 2):

$$13 \quad \begin{cases} \lambda_e = \delta_{ue} \delta_{ve} \sqrt{1 + \beta^2} \left[ \frac{1}{(\delta_{ue})^{2n} + (\beta \delta_{ve})^{2n}} \right]^{\frac{1}{2n}} \\ \lambda_f = \delta_{uf} \delta_{vf} \sqrt{1 + \beta^2} \left[ \frac{\sqrt{(\delta_{ue})^{2n} + (\beta \delta_{ve})^{2n}}}{(\delta_{ue} \delta_{uf})^n + (\beta^2 \delta_{ve} \delta_{vf})^n} \right]^{\frac{1}{n}} \end{cases} \quad (14)$$

14 The damage parameter is computed only if  $\delta_v$  is positive. Each ME is then updated with the damaged elastic  
 15 stiffness taken as the maximal value of both damage parameters computed at each extremity of the ME.

16 Finally, the displacement is linearly applied as a function of the numerical time. Each numerical test result is  
 17 obtained from a simulation run involving one hundred constant time steps  $\delta_t$ .

18 **Mesh and boundary conditions.** The bonded overlap is regularly meshed with a parametrical number  $n_{ME}$  of  
 19 bonded-beams elements. One extremity is clamped and the loading is applied under displacement (termed  $H$ ) at  
 20 the other extremity where the bending angle is fixed (see Figure 6). The applied displacement is  $H=0.074$  mm so  
 21 that the damage begins to propagate in the adhesive layer at the loaded extremity. In view of the application of  
 22 the inverse method, it is mandatory that the adhesive layer does not deform at the joint extremity where the load  
 23 is not applied. Clamping conditions avoid both peel and shear deformations.



1

2 **Figure 6.** Applied displacement  $H$  and fixed displacements for the MCB test configuration.

3 The results are not presented in this paper but a study on the influence of mesh size up to a maximal mesh  
 4 density of twenty ME per mm was performed under a pure linear elastic analysis under pure mode I ( $\alpha=\pi/2$ ).  
 5 The conclusions are that (i) the original approach and the present approach (see Appendix A) for the formulation  
 6 of the elementary stiffness matrix of ME provides exactly the same results, and (ii) the computed reaction as well  
 7 as the adhesive peak stresses do not vary at all with the mesh density.

8 **Results.** In order to assess the influence of the mesh density on the predictions from the ME model, four runs  
 9 associated with the four following mesh densities are launched: (i) one ME per mm, (ii) two MEs per mm, (iii)  
 10 four MEs per mm and (iv) eight MEs per mm. The norm of the reaction force on the loaded section of the upper  
 11 adherend as a function of the mesh density is provided in [Figure 7](#). It is shown that the model converges when  
 12 the mesh density is increased. Moreover, the maximal peel and shear stresses at  $x=L$  reached during the runs are  
 13 constant when the mesh density varies and equal to:  $S_{max}=23.6 MPa$  and  $T_{max}=19.8 MPa$ . This result is not  
 14 surprising since the load is applied under the shape of displacement at the location where the adhesive stress  
 15 evolution is observed and the stiffness matrix is updated considering the maximal value of both damage  
 16 parameters computed at each extremity of the ME.

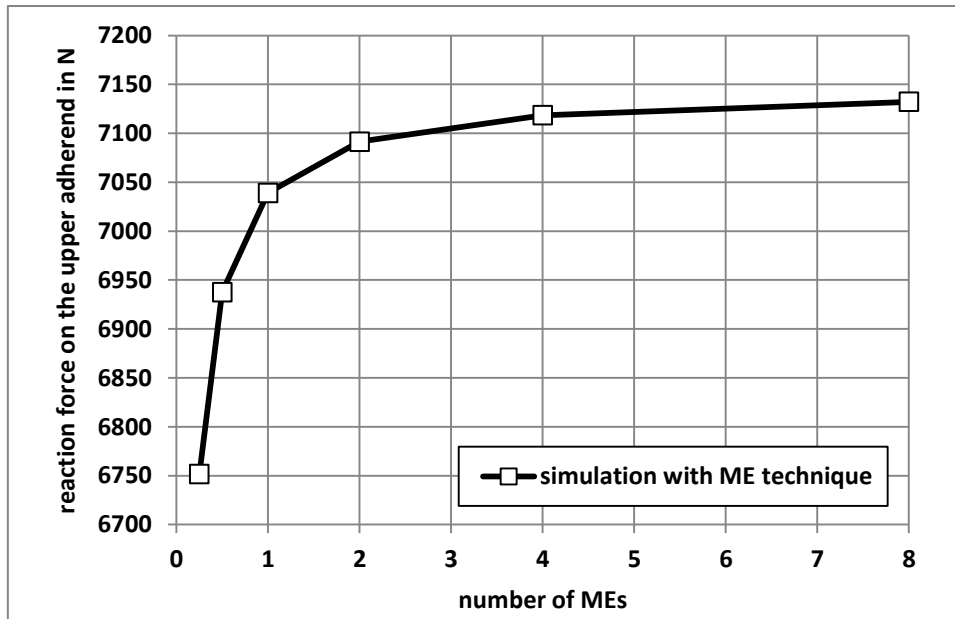
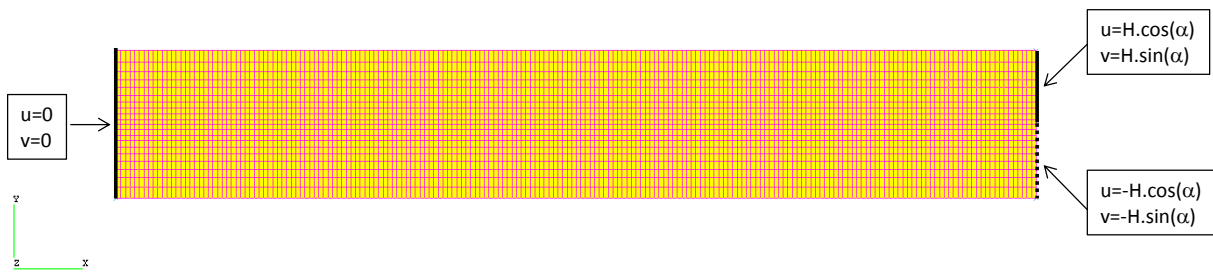


Figure 7. Norm of the reaction force on the loaded section of the upper adherend

### 2.3. Finite element model

**Mesh and boundary conditions.** A 3D FE model is developed using the FE code SAMCEF v18.1 (LMS PLM software). This model makes use of linear brick elements with eight nodes and twenty-four degrees of freedom for the adherends. A normal integration rule is selected. The adherends are assumed linear elastic. The adhesive layer is simulated through 3D quadrangular interface elements. The CZM defined in section 2.1 is applied through the Damage Interface SAMCEF material. The adhesive layer is regularly meshed along the overlap length and width, with a constant aspect ratio equal to one: all the interface elements are squared. The adherends mesh is coincident at the interface with the adhesive layer. The mesh along the thickness of adherends is distributed as it follows. The adherends are cut at their own neutral plane in two parts. A distributed mesh is applied on each part and a transition ratio equal to one is applied at the neutral plane. The size along the thickness of the last element at the neutral axis of the adherend is fifty percent larger than those of the first element at the interface with the adhesive layer. The same size ratio is applied for the second part. The mesh of two adherend parts at the neutral plane is then coincident, so that a kinematic bonding of nodes is applied. As a result, following the previous meshing method, the number of elements along the overlap drives the meshing of the full model. The boundary conditions are relevant to those applied in the previous ME model. Only one half of specimen is modelled and symmetry conditions are applied. The adherends are clamped at one extremity and loaded under displacement at the other extremity (see Figure 8). It is indicated that the boundary conditions

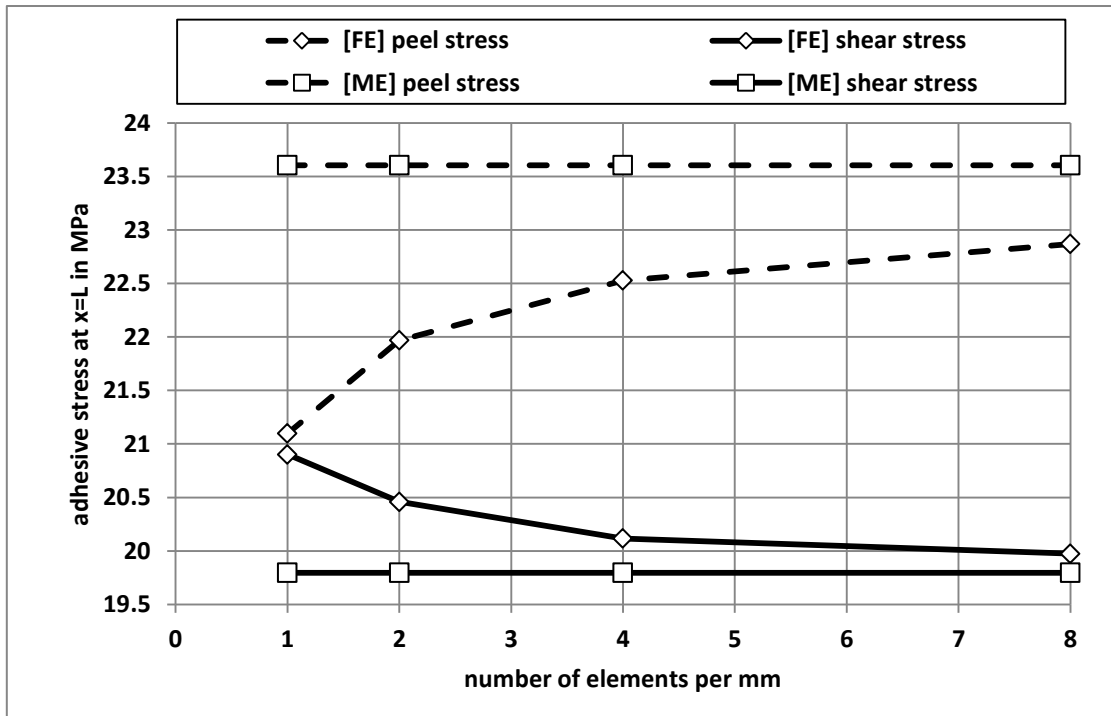
1 applied on the FE element model are relevant to those applied on the ME model. In particular, at the loaded  
 2 extremity, the longitudinal displacement at the interface with the adhesive layer is the one at the neutral axis.  
 3 **Nonlinear computation.** The nonlinear computation is based on a Newton Raphson scheme, for which the  
 4 stiffness matrix is updated at each iteration with the secant properties concerning the adhesive layer. The  
 5 computation remains geometric linear, due the level of displacements and rotation. The applied displacement is  
 6  $H=0.074\text{ mm}$  as for the simulations based on ME model. It is sufficient to apply the inverse method. As for the  
 7 simulations based on the ME model, each numerical test result is obtained from a simulation run involving one  
 8 hundred constant time steps  $\delta t$ .



9  
 10 **Figure 8.** View of the 3D FE model on the symmetry plane including the mesh (two MEs per mm) and the  
 11 boundary conditions.

12  
 13 **Results.** As for the ME model, the influence of the mesh density on the predictions from the FE model is  
 14 assessed using the same 4 mesh densities. The maximal peel and shear stresses at  $x=L$  reached during the run is  
 15 provided in [Figure 9](#) as a function of the mesh density. It is shown that these adhesive peak stresses converges  
 16 when the mesh density is increased, while tending to the adhesive peak stresses predicted by the ME model. For  
 17 a mesh density of eight element per mm, the relative difference in the FE model prediction from the ME model  
 18 prediction is -3.11% in peak peel stress and +0.90% in peak shear stress. The evolution of the adhesive peel  
 19 (shear) stress as a function of the opening (sliding) displacement at  $x=L$  for the FE and ME models with a mesh  
 20 density of eight elements per mm is provided in [Figure 10](#) ([Figure 11](#)). A very good agreement is then shown  
 21 between the predictions of the FE and ME models.

22



1

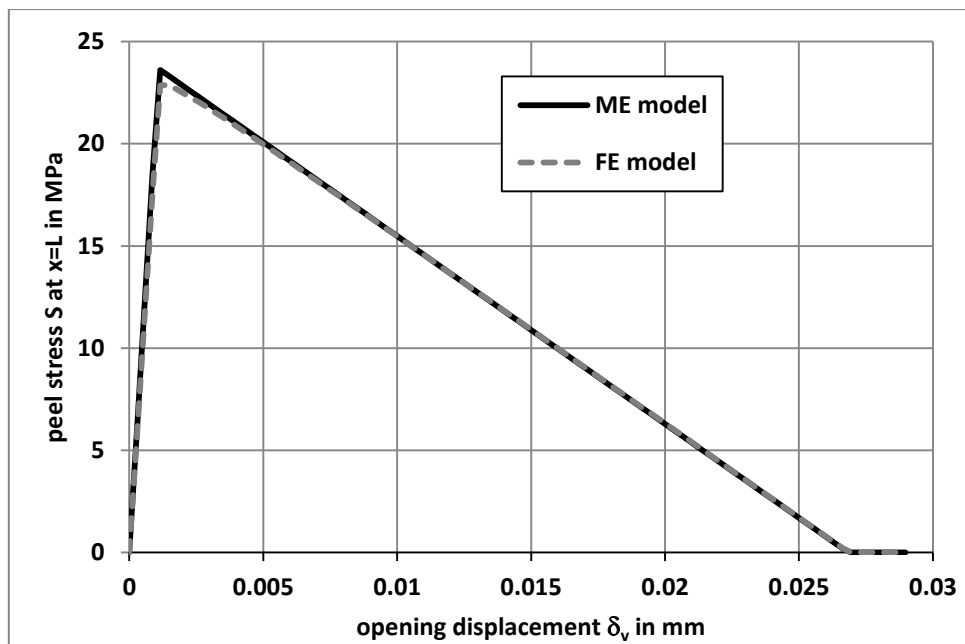
2 **Figure 9.** Maximal peel and shear stresses at  $x=L$  reached during the run as a function of the mesh density for the  
 3 FE and ME models.

4

5

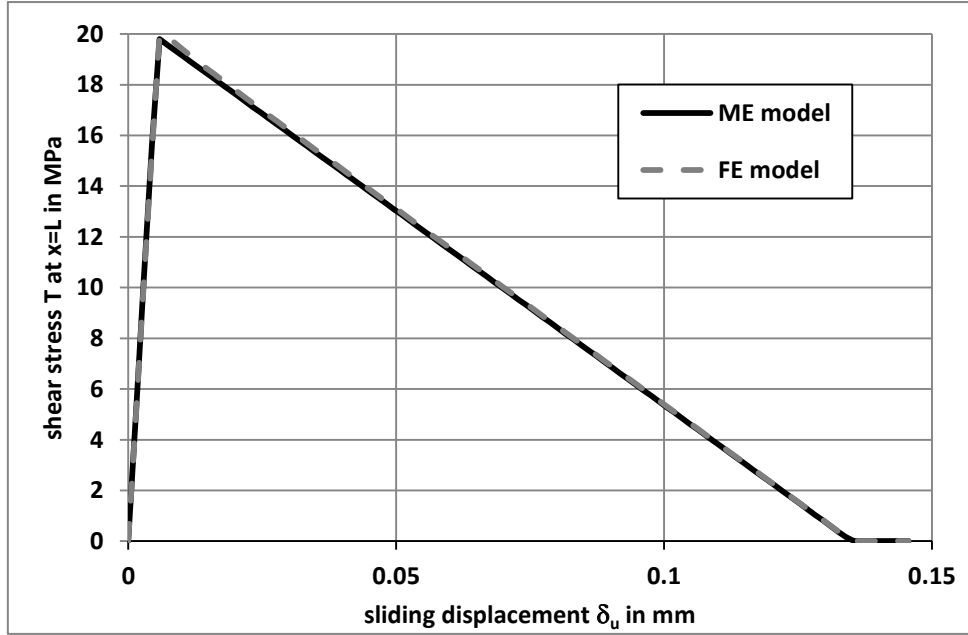
6

7



8

1 **Figure 10.** Evolution of the adhesive peel stress as a function of the opening displacement at  $x=L$  for the FE and  
 2 ME models with a mesh density of eight elements per mm.



4  
 5 **Figure 11.** Evolution of the adhesive shear stress as a function of the sliding displacement at  $x=L$  for the FE and  
 6 ME models with a mesh density of eight elements per mm.

7  
 8 **2.4. Application of the inverse method**

9 The inverse method is applied on the predictions of the ME model with a mesh density of eight element per mm.  
 10 Firstly, the J-integral parameter at  $x=L$  has to be computed according to Eq. (2). Taking benefit from the elevated  
 11 number of computation time, a simple numerical integration is then performed as:

12 
$$J(t_f) = \sum_{i=1}^{i=f} T(t_i) [\delta_u(t_i) - \delta_u(t_{i-1})] + \sum_{i=1}^{i=f} S(t_i) [\delta_v(t_i) - \delta_v(t_{i-1})] \quad (15)$$

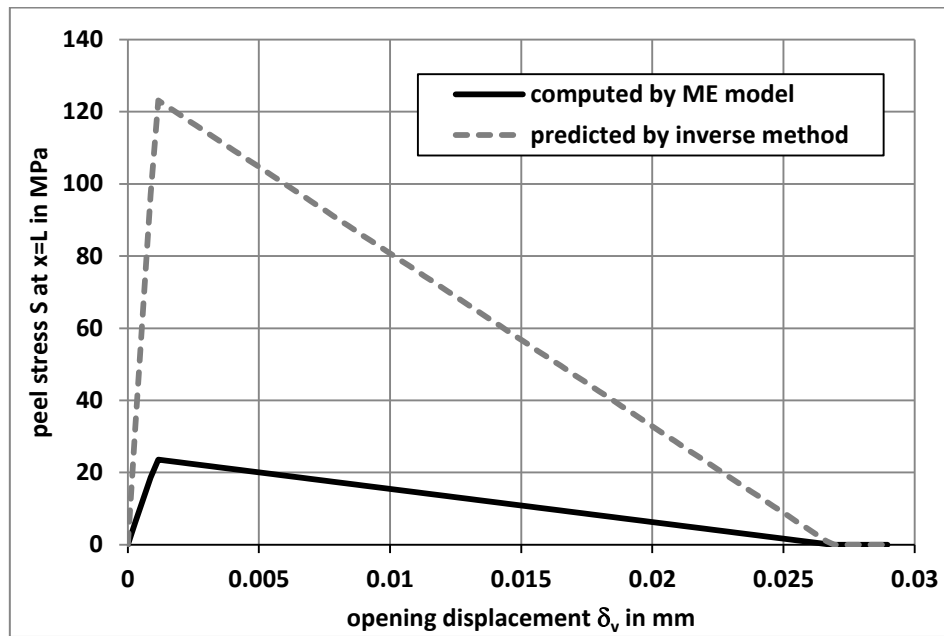
13 where  $t_i$  is the  $i^{\text{th}}$  computation time,  $t_f$  is the las computation time and  $t_0$  is equal to zero. It is indicated that this  
 14 computation of the J-integral is valid in the abscissa  $x=L$  only and at any time, because (i) the applied loading on  
 15 the neutral line in terms of  $\delta_u$  and  $\delta_v$  is the same as the one seen at the interface in  $x=L$  ( $\theta=0$ ) and (ii) the applied  
 16 loading is proportional at any time. As a result, the mixed mode parameter  $\beta$  is constant at any time in  $x=L$  and  
 17 the shear (peel) stress is only dependent on  $\delta_u$  ( $\delta_v$ ) at the given constant  $\beta$ .

18 Secondly, the adhesive stresses are computed according to Eq. (5) and Eq. (6). The required differentiation of the  
 19 J-integral parameter is obtained by taken the slope between two consecutive times:

$$\begin{cases} S(\delta_v(t)) = \frac{J(t)-J(t-\delta_t)}{\delta_v(t)-\delta_v(t-\delta_t)} \\ T(\delta_u(t)) = \frac{J(t)-J(t-\delta_t)}{\delta_u(t)-\delta_u(t-\delta_t)} \end{cases} \quad (16)$$

2 The evolution of the adhesive peel (shear) stress as a function of the opening (sliding) displacement at  $x=L$  as  
3 computed by the ME model with a mesh density of eight elements per mm and predicted by the inverse method  
4 is provided in Figure 12 (Figure 13). It is shown that the predictions of the inverse method does not fit those of  
5 the ME models. It is then concluded that the considered CZM is an example for which the inverse method fails  
6 to predict the adhesive peel and shear stresses under mixed-mode. This example is not a general proof for this  
7 type of CZM. However, the main fact is that the application of the inverse method associated with particular  
8 types of CZM could lead to incorrect behavior assessment.

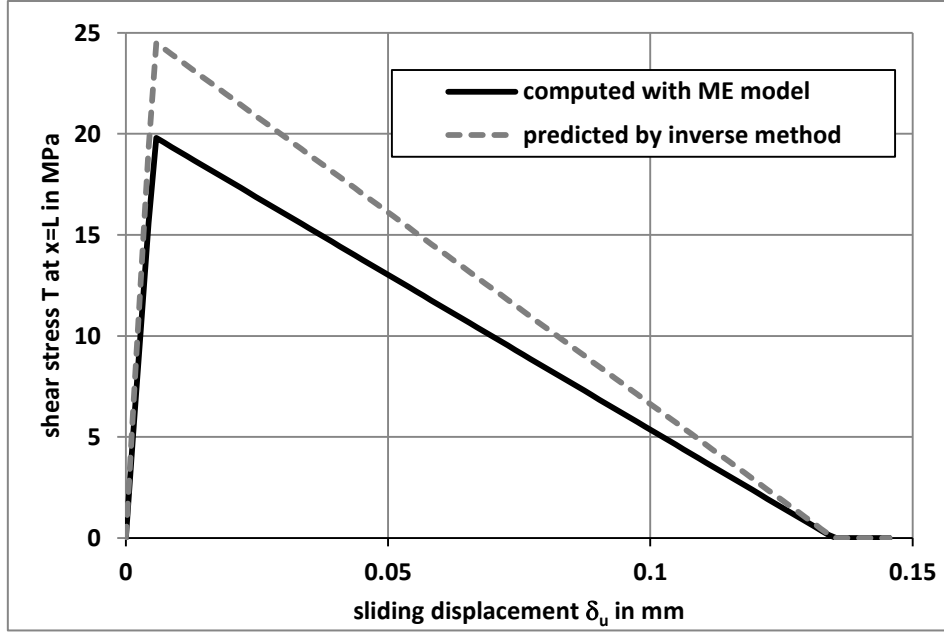
9



10

11 **Figure 12.** Evolution of the adhesive peel stress as a function of the opening displacement at  $x=L$  as computed by  
12 the ME model with a mesh density of eight elements per mm and predicted by the inverse method.

13



1  
2 **Figure 13.** Evolution of the adhesive shear stress as a function of the sliding displacement at  $x=L$  as computed by  
3 the ME model with a mesh density of eight elements per mm and predicted by the inverse method.  
4

#### 5 2.5. Description of the Direct Method

6 This method is presented in (Lélias 2016). It is based on the measurement around the crack tip of the  
7 displacement of the neutral axis according to the x-axis and the y-axis. Contrary to the inverse method, no spatial  
8 integration of equilibrium equations is required.

9 In the case of pure mode I loading, the adhesive shear stress vanishes so that the local equilibrium of adherends  
10 can be reduced to the following set of differential equations for  $j=1,2$ :

$$11 \begin{cases} \frac{dN_j}{dx} = 0 \\ \frac{dV_j}{dx} = (-1)^{j+1} bS \\ \frac{dM_j}{dx} + V_j = 0 \end{cases} \quad (17)$$

12 As a result, it comes:

$$13 S = (-1)^j \left[ -\frac{B_j}{b} \frac{d^3 u_j}{dx^3} + \frac{D_j}{b} \frac{d^4 w_j}{dx^4} \right] \quad (18)$$

14 Using the constitutive relationship, the adhesive peel stress can be expressed as:

$$15 S = (-1)^j \frac{D_j}{b} \frac{d^4 w_j}{dx^4} \quad (19)$$

16 In the case of pure mode II loading, the adhesive peel stress vanishes so that the local equilibrium of adherends  
17 can be reduced to the following set of differential equations for  $j=1,2$ :

$$1 \quad \begin{cases} \frac{dN_j}{dx} = (-1)^j bT \\ \frac{dV_j}{dx} = 0 \\ \frac{dM_j}{dx} + V_j + bh_jT = 0 \end{cases} \quad (20)$$

2 As a result, it comes:

$$3 \quad T = (-1)^j \left[ \frac{A_j}{b} \frac{d^2 u_j}{dx^2} - \frac{B_j}{b} \frac{d^3 w_j}{dx^3} \right] \quad (21)$$

4 Using the constitutive relationships, the adhesive shear stress can be expressed as:

$$5 \quad T = (-1)^j \frac{A_j}{b} \frac{d^2 u_j}{dx^2} \quad (22)$$

6 In the case of mixed-mode I/II loading, the local equilibrium of adherends is given by Eq. (5). The following  
7 expressions for the adhesive peel and shear stresses are obtained:

$$8 \quad S = \left[ (-1)^j \frac{D_j}{b} - h_j \frac{B_j}{b} \right] \frac{d^4 w_j}{dx^4} + \left[ h_j \frac{A_j}{b} - (-1)^j \frac{B_j}{b} \right] \frac{d^3 u_j}{dx^3} \quad (23)$$

$$9 \quad T = (-1)^j \left[ \frac{A_j}{b} \frac{d^2 u_j}{dx^2} - \frac{B_j}{b} \frac{d^3 w_j}{dx^3} \right] \quad (24)$$

10 The same hypotheses as for the ME model are used for the direct method, so that its application on numerical  
11 test results with a suitable post processing method provides predictions exactly corresponding to those of ME. A  
12 design of experiments is then developed to investigate the main factors influencing the predictions of the direct  
13 method.

14

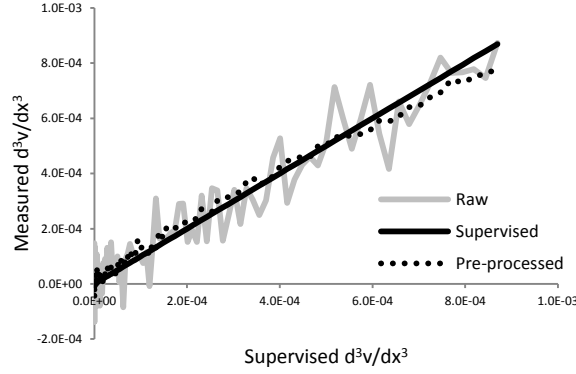
### 15 **3. Assessing our methodology of derivatives of deflection with DIC experimental parameters**

#### 16 *3.1. Signal processing of the 3<sup>rd</sup> order derivative of the deflection*

17 Within the framework of the direct method, the evolution of the adhesive stresses can be theoretically derived  
18 from the measurement at the crack tip of the second and third order derivative of the upper adherend bending  
19 angle and of the derivative of the upper adherend longitudinal displacement at neutral axis (see section 2.5).

20 Since the raw differentiation of noised experimental results can lead to the rise of important numerical  
21 singularities, a particular attention has to be given to the correct evaluation of these successive derivatives. Data  
22 pre-processing is then highly needed to reduce experimental noises (see Figure 14). The data pre-processing  
23 algorithm used to reduce experimental noises from the measured upper and lower adherends displacement fields  
24 lies on the optimal sub-rank approximation (OSRA) based on singular value decomposition (SVD), and is  
25 related to signal processing techniques that are commonly referred to as SVD signal enhancement methods,  
26 reduced-rank signal processing or more simply subspace methods (Andrews and Patterson 1973). The detailed

1 presentation of the data pre-processing is not given in detail in this paper; a summarized description can be found  
 2 in the [Appendix B](#).



3  
 4 **Figure 14.** Comparison of the 3<sup>rd</sup> order derivative of the deflection of the neutral fiber of the upper adherend  
 5 obtained from raw and pre-processed experimental results.

### 7 3.2. Supervised experiments using virtual fields

8 To characterize the ability of the suggested data pre-processing and differentiation algorithm to determine the  
 9 successive derivatives of the adherend-to-adherend displacement field with sufficient accuracy, we propose to  
 10 use supervised virtual fields. It refers to the data pre-processing and data differentiation of a displacement field  
 11 that is virtually generated so that the evolution of its successive derivatives is known in advance of the  
 12 experiment. For simplification purpose, the comparison between the supervised data and those obtained from the  
 13 data processing will be made in terms of the 3rd and 4th order derivatives of the transverse displacement of the  
 14 adherend neutral axis only. However the results are similar with other derivatives

15 The virtual displacement field is generated using Matlab® R2012b and resumes the kinematic of a classical  
 16 Euler-Bernoulli's beam in coupled in-plane tension/flexion, so that:

$$17 \begin{cases} u(x, y, t) = u(x, y = 0, t) - y \frac{\partial v(x, y=0, t)}{\partial x} \\ v(x, y, t) = v(x, y = 0, t) \end{cases} \quad (25)$$

18 where the evolutions of  $u(x, y=0, t)$  and  $v(x, y=0, t)$  are arbitrary fixed as:

$$19 \begin{cases} u(x, y = 0, t) = e^{-0.005tx} \\ v(x, y = 0, t) = e^{-0.15tx} \end{cases} \quad (26)$$

20 To model the effect of experimental noises, the virtual displacement field described in [Eq. \(25\)](#) and [Eq. \(26\)](#) is  
 21 then degraded by adding a normal (Gaussian) noise using the `normrand(0,σ)` Matlab® function, where  $0$  refers to  
 22 the prescribed zero mean value and  $\sigma$  to the configurable standard deviation of the normal (Gaussian) noise  
 23 distribution.

1 In order to test for the linear dependency between the successive derivatives of the supervised data and those  
 2 obtained from the fitted polynomial series, the Pearson product-moment correlation coefficient is used:

$$3 \quad r = \frac{n(\sum xy) - (\sum x)(\sum y)}{\sqrt{[n\sum x^2 - (\sum x)^2][n\sum y^2 - (\sum y)^2]}} \quad (27)$$

4 where  $x$  refers to the set of supervised data,  $y$  to the set of simulated data and  $n$  to the total number of data pairs.

5

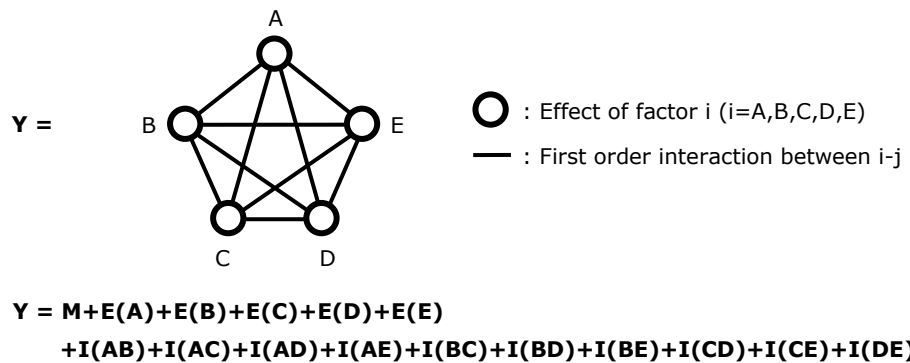
### 6 3.3. Chosen DOE and justification

7 A full factorial Design of Experiments (DoE) consists in the following: (i) vary one factor at a time, (ii) perform  
 8 experiments for all levels and combination of levels for all factors, (iii) hence perform a large number of  
 9 experiments ( $N$ ), (iv) so that all effects and interactions are captured. Let  $k$  be the number of factor,  $n_i$  the number  
 10 of levels of the  $i^{th}$  factor and  $p$  the number of replications to determine the impact of the measurement dispersion.

11 The total number of experiments  $N$  of a full factorial DoE is then:

$$12 \quad N = p(\prod_{i=1}^k n_i) \quad (28)$$

13 Here is considered a full factorial DoE of five factors with respectively 3x3x3x3x2 levels, so that the linear  
 14 Taguchi's graph of effects and interactions can be represented in the form of Figure 15.



15

16 **Figure 15.** Linear Taguchi's graph of main effects and interactions.

17

18 In Figure 15, the main effects and interactions are represented, termed respectively  $E(i)$  and  $I(ij)$ , of factors  $i, j = A,$   
 19  $B, C, D$  and  $E$  onto the objective function that is  $r^2$ . Each experiment is replicated 15 times to capture the impact  
 20 of the measurement dispersion, so that the total number of experiments is  $(3 \times 3 \times 3 \times 3 \times 2) \times 15 = 2430$ . The different  
 21 factor levels are given in Table 3.

22

23

24

1

Table 3. Factor versus levels matrix.

	SNR <sup>-1</sup> (A)	x=y (B)	t (C)	Degree (D)	Model (E)
Low (-1)	0.00175	201	51	4	1
Medium (0)	0.00350	401	101	6	N.A
High (+1)	0.00700	801	201	8	2

2

3 where *SNR* refers to the simulated Signal-to-Noise ratio, *x=y* to the spatial resolution of each displacement field  
4 instantaneous image, *t* to the number of instantaneous images taken during the experiment (i.e. thereafter  
5 referred as the temporal resolution), *Degree* to the degree of the polynomial series used to fit/differentiate the  
6 neutral fiber transverse displacement and *Model* to the model used for minimizing the vertical deviation with  
7 experimental data in the sense of the least squares method (1 means fitting independently on  $v(x)$  and on  
8  $\theta(x)=dv(x)/dx$ , 2 means fitting simultaneously  $v(x)$  and  $\theta(x)=dv(x)/dx$ ).

9

#### 10 3.4. Synthesis of the results

11 The initial SNR appears as a key parameter in increasing the accuracy of measuring the successive derivatives of  
12 the upper adherend displacement field (see [Figure 16-\(a\)](#)), then suggesting that a significant attention has to be  
13 given into reducing the noise of the measured signal before any pre-processing of the data. This can be achieved  
14 in various ways so that it results in improving the overall quality of the displacement measures.

15

16

17

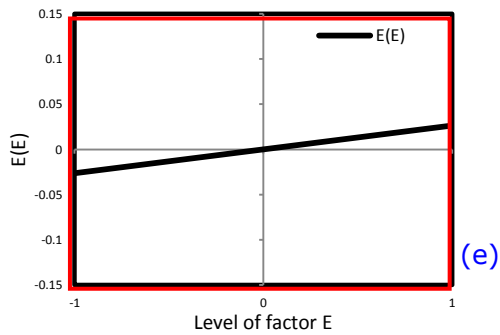
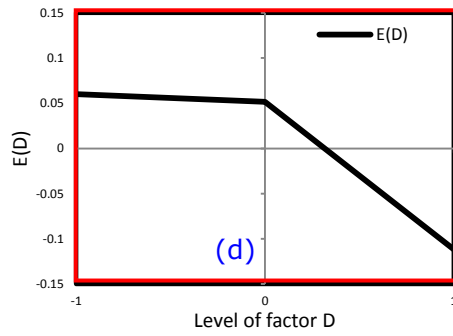
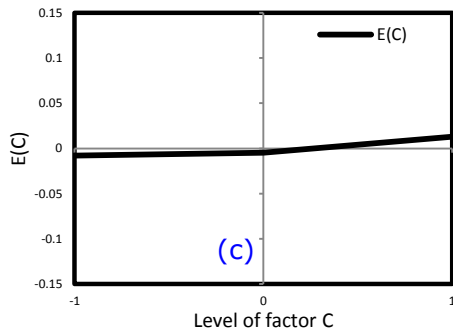
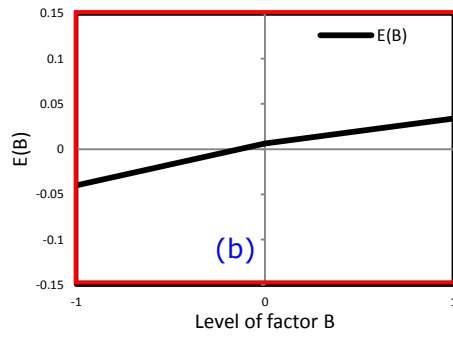
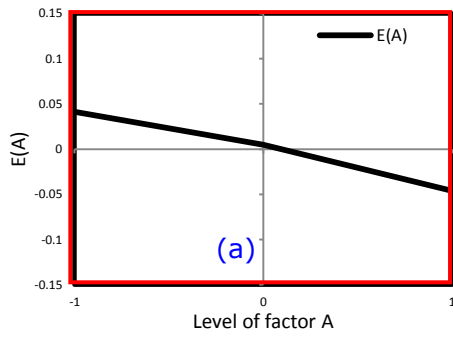
18

19

20

21

22



1

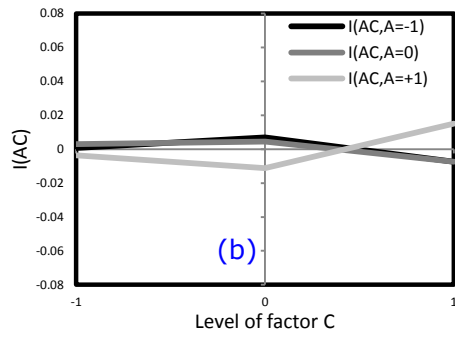
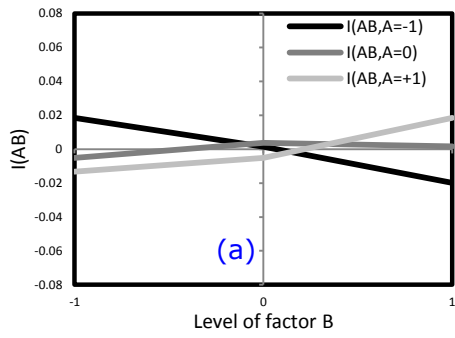
2

3

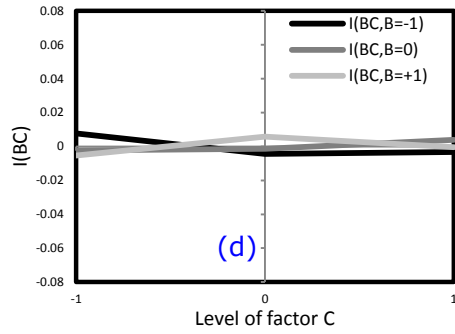
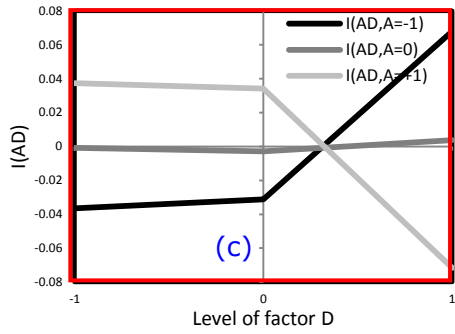
4 **Figure 16.** Effect of factor  $i$  ( $i=A,B,C,D,E$ ) on the correlation coefficient  $r^2$ . Influence of the experimental  
 5 (algorithmic) parameters on the accuracy of the experimental measures. Red= Significant effects. Black=  
 6 Negligible effects.

7

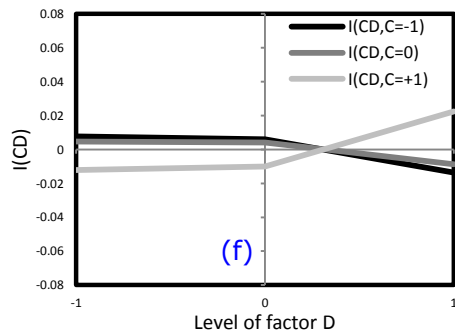
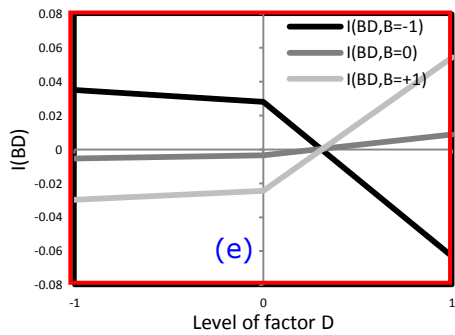
8 The spatial resolution of the instantaneous images of the upper adherend displacement field also appears as a key  
 9 parameter in increasing the accuracy of the estimation of the successive derivatives of the upper adherend  
 10 displacements (see [Figure 16-\(b\)](#), [Figure 17-\(e\)](#) and [Figure 17-\(h\)](#)). A particular attention has then to be given to  
 11 measuring the displacements of the upper adherend with a sufficient enough spatial resolution.



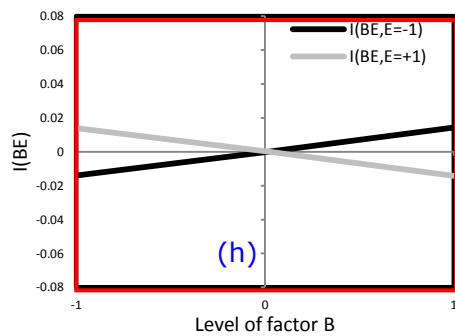
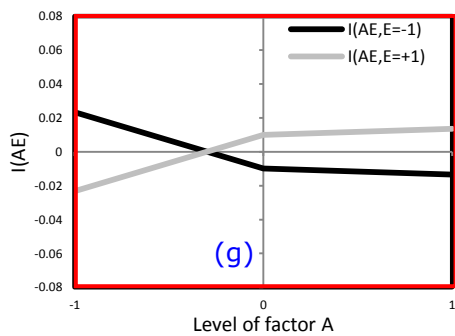
1



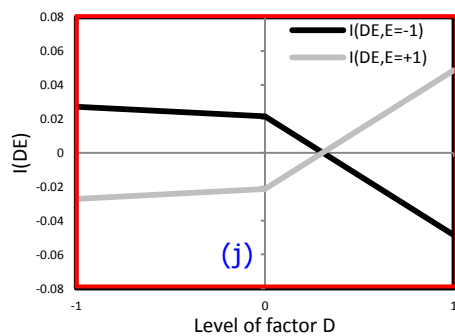
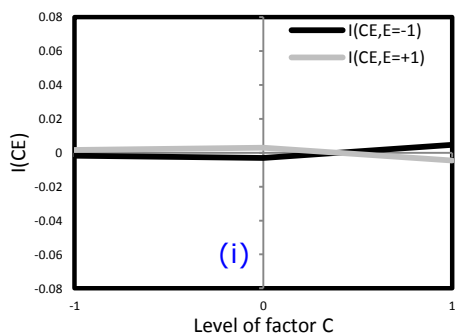
2



3



4



5

1 **Figure 17.** First order interaction between factors  $i-j$  ( $i,j=A,B,C,D,E$ ) on the correlation coefficient  $r^2$ . Influence  
2 of the experimental (algorithmic) parameters on the accuracy of the experimental measures. Red= Significant  
3 interactions. Black= Negligible interactions.

4  
5 On another side, the time resolution (i.e. number of images of the upper adherend displacement field taken  
6 during the experiment) appears as negligibly influencing the accuracy of the estimation of the successive  
7 derivatives of the upper adherend displacements (see [Figure 16-\(c\)](#), [Figure 17-\(b\)](#), [Figure 17-\(d\)](#), [Figure 17-\(f\)](#)  
8 and [Figure 17-\(i\)](#)). Thus its own effect as well as its respective interactions with other factors can be legitimately  
9 neglected at first sight.

10 Similarly to the initial SNR or the spatial resolution of the displacement images, the degree of the polynomial  
11 series used for fitting/differentiating the pre-processed displacements also appears as a parameter that has to be  
12 chosen with extreme caution. Indeed, although increasing the degree of the polynomial series from 4 to 6 appears  
13 as negligibly influencing the overall accuracy of the measure, increasing it from 6 to 8 results in a serious  
14 degradation of the accuracy of the measure (see [Figure 16-\(d\)](#)). This degradation of the accuracy of the  
15 measurement using high order polynomials is a well-known issue, and is due to the oscillation of the polynomial  
16 series around the experimental set of data points for increasing degrees (i.e. Runge's phenomenon). A particular  
17 attention has then to be given in choosing the best compromise between fitting the experimental data points  
18 using high order polynomials functions and preserving the overall accuracy of the measurement of its successive  
19 derivatives.

20 Finally, the choice of the Moore-Penrose pseudo inverse model for minimizing in the sense of the least squares  
21 method the vertical deviation between the polynomial function (i.e. used for fitting/differentiating the set of  
22 experimental data points) and the experimental data points themselves appears as a worthwhile way of  
23 influencing the accuracy of the measured displacement derivatives (see [Figure 16-\(e\)](#)). It is then suggested that  
24 simultaneously accounting for both  $v(x)$  and  $\theta(x)=dv(x)/dx$  when fitting/differentiating the experimental set of  
25 data points significantly increases the accuracy of the measurement.

26

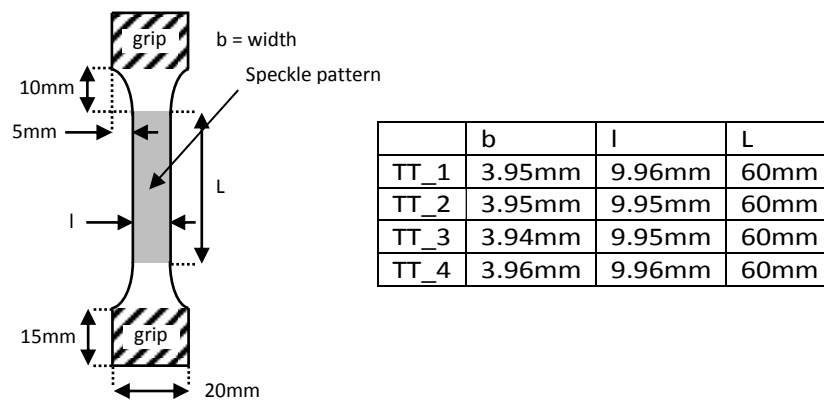
## 27 **4. Experimental test campaign**

28 The entire test campaign is performed on an electro-mechanical test machine (Ref: Instron AI735-1325).

### 29 *4.1. Adherend bulk specimens*

1 Each specimen is manufactured from a laminated aluminum-magnesium-silicon alloy (6060 series). A total of  
 2 three specimens are tested. The manufactured specimens are measured before the tests (see Figure 18). The  
 3 evolution of both the applied load and the resulting displacement are measured using the build-in machine load  
 4 and displacement cells. The loading speed is fixed at 0.5mm/min. The evolution of the specimen displacement  
 5 field is measured using the Digital Image Correlation (DIC) technique (see Figure 19). Both the evolution of the  
 6 axial deformation and the Poisson's ratio of the samples are computed from the evolution of the specimen  
 7 displacement field. The specimens are displacement loaded using the build-in machine displacement command  
 8 instruction. The results obtained in terms of (a) the axial stress-strain evolution law and (b) the evolution of the  
 9 measured Poisson's ratio as a function of the axial deformation in Figure 20. The aluminum alloy exhibits two  
 10 distinct phases. The first one, the linear elastic phase, appears as extremely limited compared to the whole  
 11 deforming capability of the material (i.e. ~3% of the whole deforming capability of the material). The second  
 12 phase, the plasticization phase, appears on another side as extremely important (i.e. ~97% of the whole  
 13 deforming capability of the material). To model the effective stress-strain evolution law of each adherend, it is  
 14 then decided to fit a trilinear elastic-plastic evolution law onto the results obtained (see Figure 21). The material  
 15 law identified is provided in Table 4. A Poisson's ratio of 0.35 is considered.

16

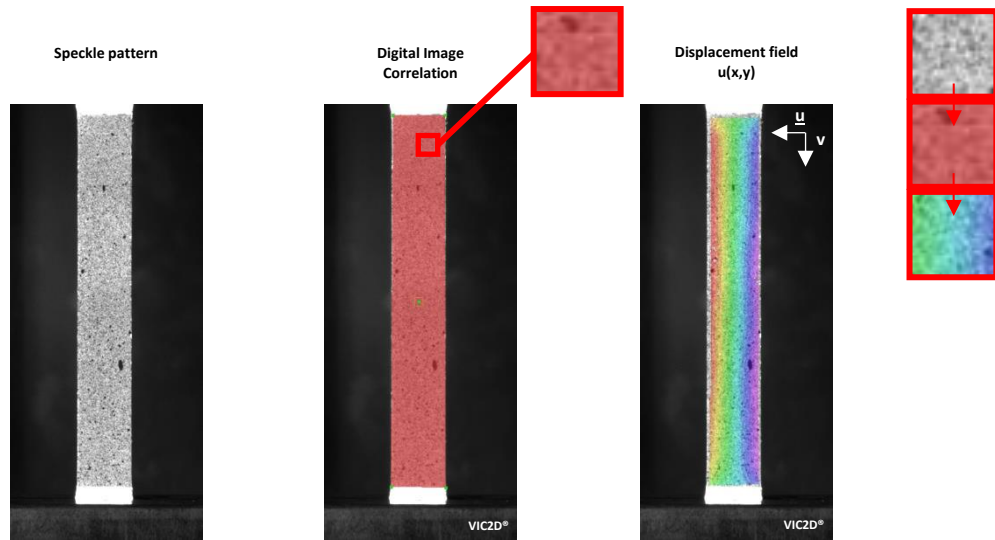


17

18

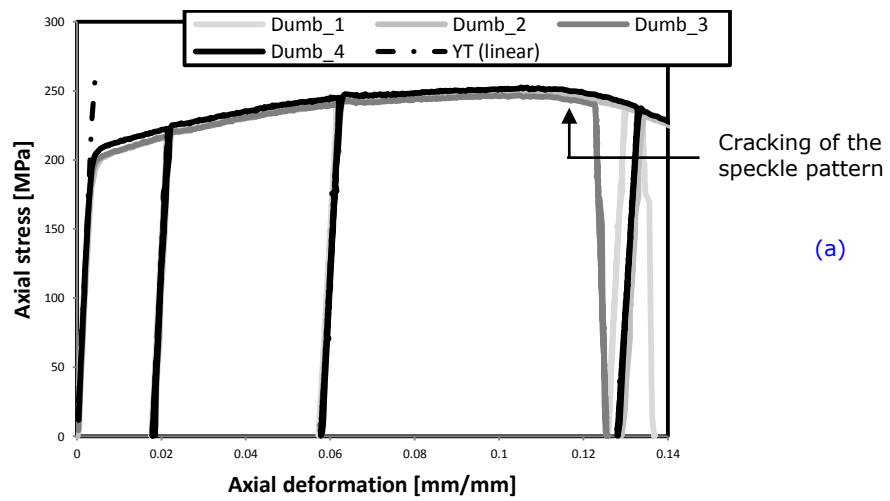
19

Figure 18. Geometry of the aluminum bulk specimens.

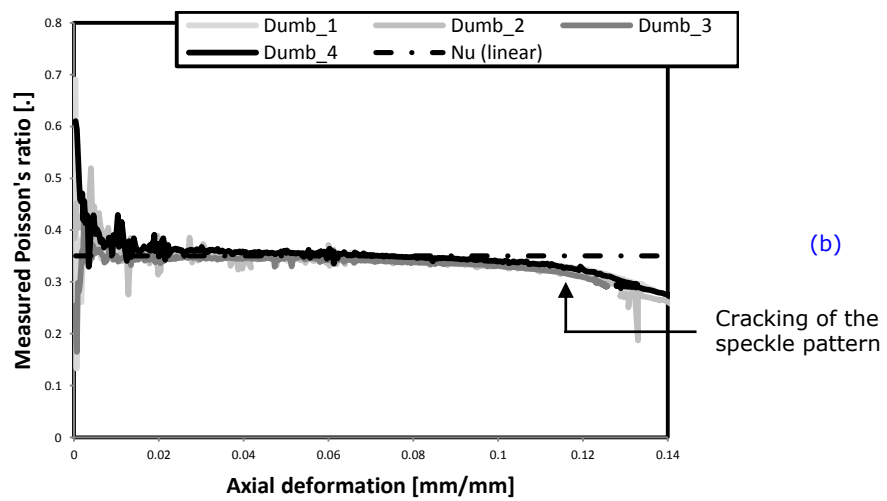


1  
2  
3  
4

Figure 19. Measuring the displacement field of aluminum bulk specimens using Digital Image Correlation (DIC) techniques.



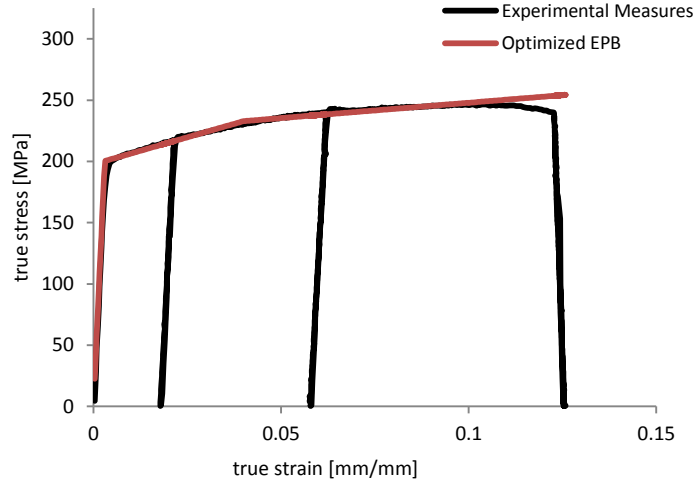
5



6

1 **Figure 20.** Experimental characterization for aluminum bulk specimens in terms of axial stress-strain evolution  
 2 law (a) and evolution of the measured Poisson's ratio (b). YT is the Young's modulus.

3  
 4



5  
 6 **Figure 21.** Experimental characterization of aluminum bulk specimens. Representation for the optimized  
 7 trilinear elastic plastic stress-strain evolution law.

8  
 9

**Table 4.** Definition of aluminum bulk material law identified.  $\sigma$ = true stress.  $\varepsilon$ = true strain.

	Elastic	Plastic 1	Plastic 2
Model (EPB)	$\sigma(\varepsilon) = E\varepsilon$	$\sigma(\varepsilon) = \sigma_1 + E_{T,1}(\varepsilon - \varepsilon_1)$	$\sigma(\varepsilon) = \sigma_2 + E_{T,2}(\varepsilon - \varepsilon_2)$
Parameters	$E = 66000MPa$	$E_{T,1} = 8800MPa$ $\sigma_1 = 200.31MPa$ $\varepsilon_1 = 0.003035$	$E_{T,2} = 250MPa$ $\sigma_2 = 232.84MPa$ $\varepsilon_2 = 0.04$
Validity	$0 \leq \varepsilon \leq \varepsilon_1$	$\varepsilon_1 \leq \varepsilon \leq \varepsilon_2$	$\varepsilon_2 \leq \varepsilon$

10  
 11 **4.2. Adhesive joint specimens**

12 **4.2.1. Overview of the experimental setting**

13 The adhesive used is the SAF30 MIB adhesive from AEC Polymers / BOSTIK (ARKEMA Group). It is a  
 14 methacrylate-based two-component adhesive paste. In order to enhance the adhesion properties between the  
 15 adhesive layer and each adherend before bonding, both adherends are cleaned using the AEC Polymers T700 dry  
 16 cleaning spray. In order to ensure a constant adhesive thickness along the overlap, two calibrated anti-adhesive  
 17 tapes are stuck at each side of the bonded overlap (see **Figure 3**). The dimensions of each specimen are  
 18 controlled after bonding (see **Table 5**). The applied load, the resulting displacement and the adherend-to-

1 adherend displacement field at crack tip are measured during the tests. The evolution of both the applied load  
 2 and the resulting displacement are measured using the build in machine load and displacement cells. The load  
 3 speed is  $0.5 \text{ mm}\cdot\text{min}^{-1}$ . The evolution of the adherend-to-adherend displacement field is measured using the DIC  
 4 technique (see [Figure 22](#) and [Figure 23](#)). The pure mode deformations of the adhesive layer are computed from  
 5 the relative displacement of the adherends neutral fibers (see [Figure 24](#)). Both DIC and build-in machine  
 6 measures are synchronized using an analogical-to-numerical National Instrument acquisition card, so that it  
 7 facilitates the processing of the adhesive CZM constitutive relationships. The mechanical stiffness of the tensile  
 8 test machine is characterized so that the resulting displacement measured by the build-in machine displacement  
 9 cell is corrected to fit the true displacement of the adhesive test specimens. Four specimens of each configuration  
 10 (e.g. ENF, DCB, MMB and SLJ) are tested. The SLJ specimens are tested for relevance assessment purposes  
 11 only. Correlations between experimental and numerical force versus resulting displacement curves are used to  
 12 assess the ability of the direct approach to characterize the CZM properties. A particular emphasis is given to the  
 13 ability of the suggested approach to provide both the experimental stiffness and the maximum load bearing  
 14 capability of each adhesive specimen. All the numerical tests presented in this paper are based on the simplified  
 15 stress analyses using ME, already presented in details in ([Lélias et al. 2015](#)).

16

17

[Table 5](#). Controlled geometries of the ENF, DCB, MMB and SLJ joint specimens.

	a	L	l	t	e	b
ENF	29.82mm	71.43mm	N.A.	3.96mm	0.230mm	22.0mm
DCB	30.69mm	70.0mm	N.A.	3.96mm	0.180mm	22.0mm
MMB	30.21mm	70.89mm	N.A.	3.96mm	0.180mm	22.0mm
SLJ	N.A.	51.4mm	29.35mm	3.96mm	0.120mm	22.0mm

18

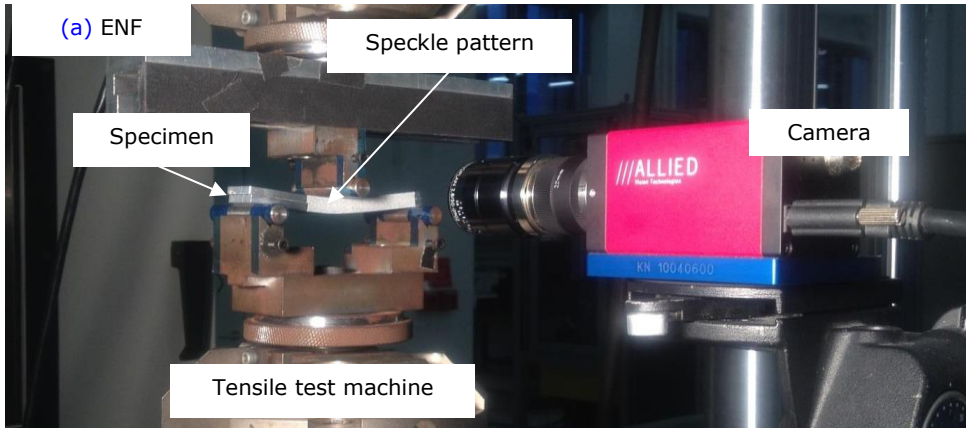
19

20

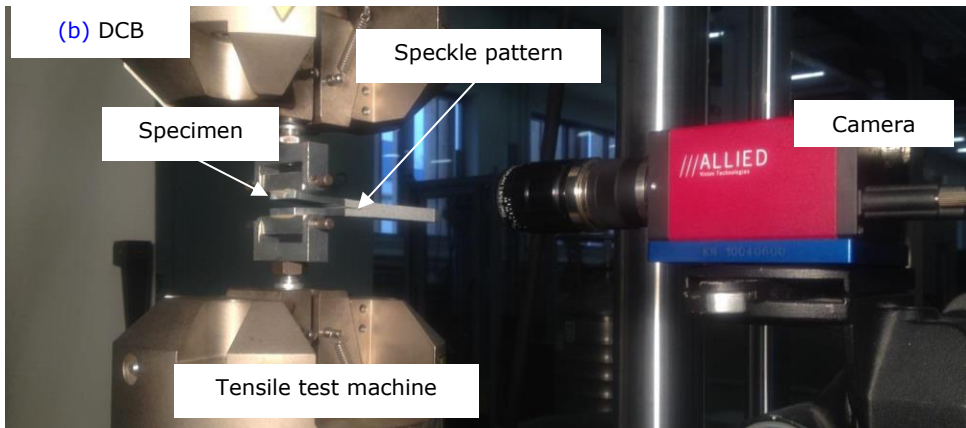
21

22

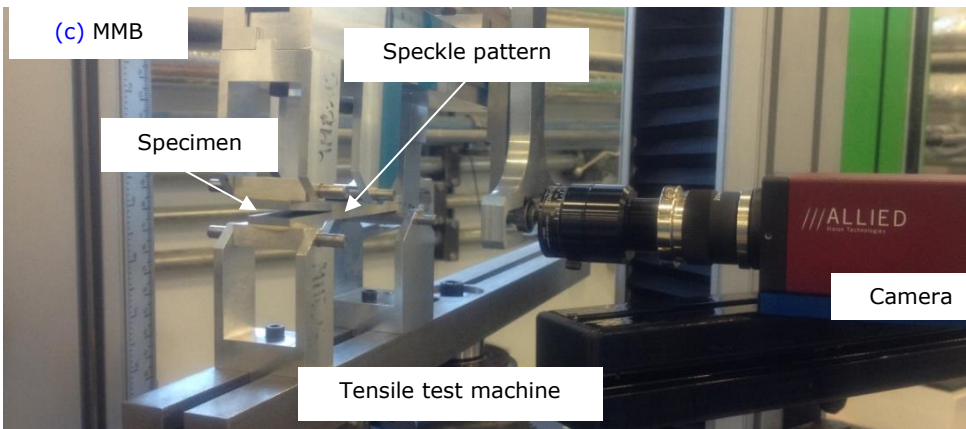
1  
2



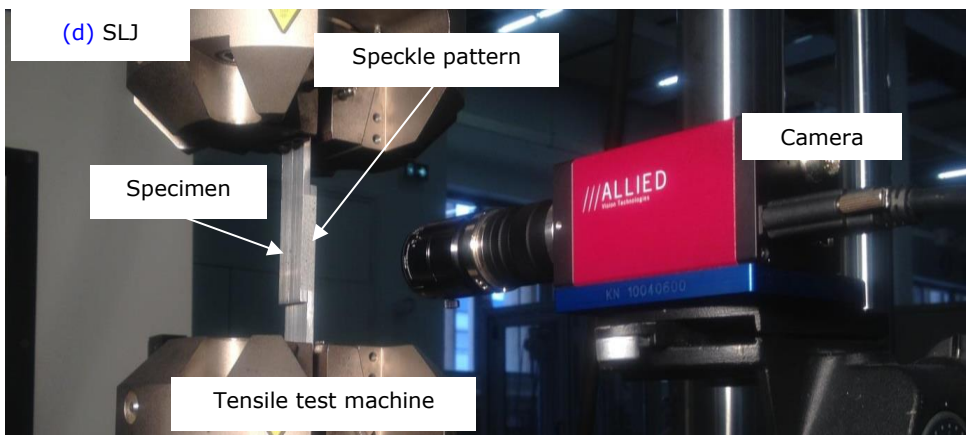
3  
4



5  
6

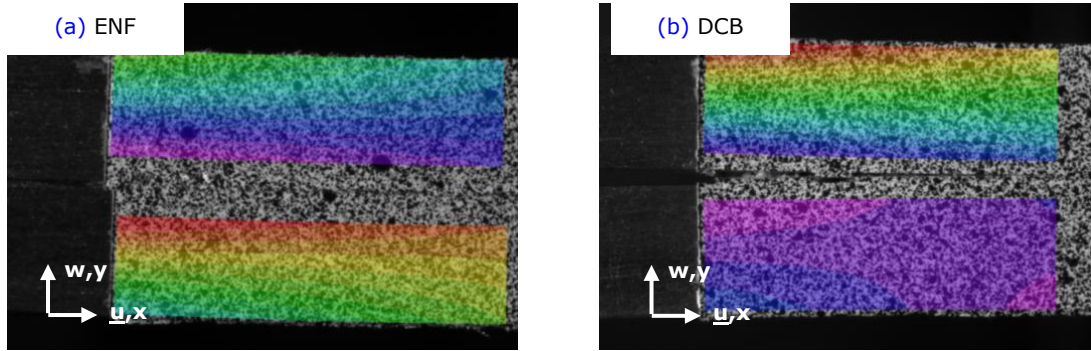


7  
8



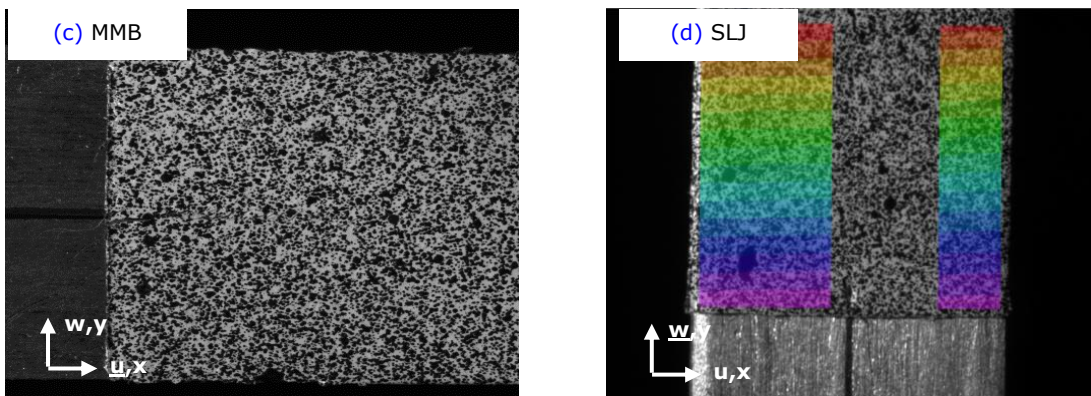
1 **Figure 22.** Experimental monitoring of the adherend-to-adherend displacement field using Digital Image  
 2 Correlation (DIC) techniques. (a) End Notched Flexure (ENF) joint specimen. (b) Double Cantilever Beam  
 3 (DCB) joint specimen. (c) Mixed-Mode Bending (MMB) joint specimen. (d) Single-Lap Joint (SLJ) joint  
 4 specimen

5



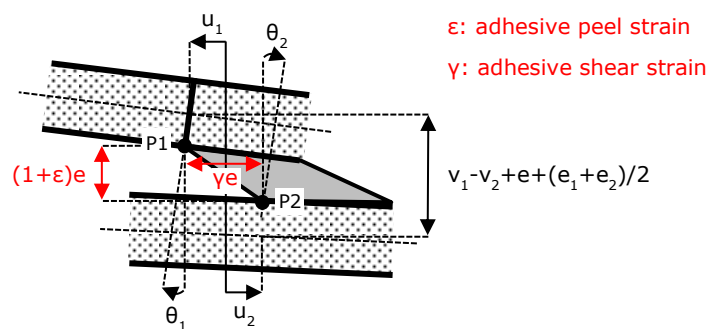
6

7



8

9 **Figure 23.** Experimental monitoring of the adherend-to-adherend displacement field using Digital Image  
 10 Correlation (DIC) techniques. (a) End Notched Flexure (ENF) joint specimen. (b) Double Cantilever Beam  
 11 (DCB) joint specimen. (c) Mixed-Mode Bending (MMB) joint specimen. (d) Single-Lap Joint (SLJ) joint  
 12 specimen.

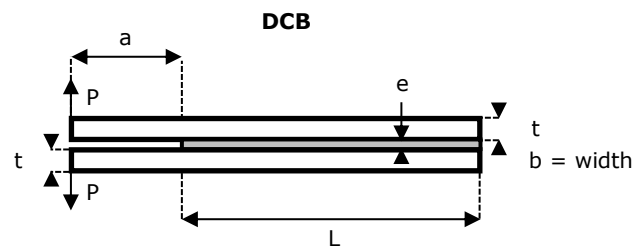


13

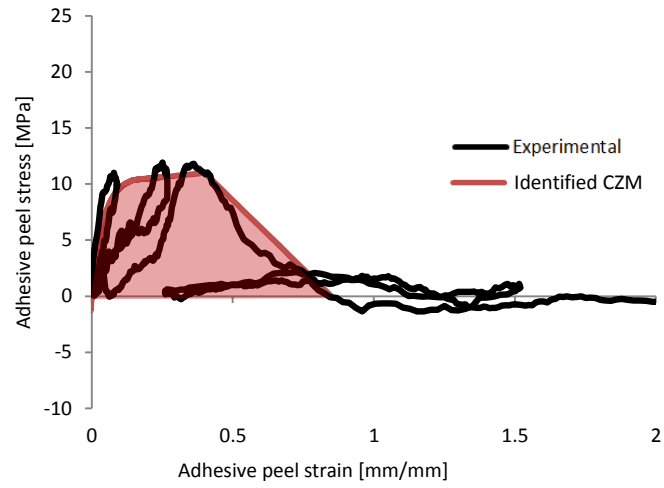
1 **Figure 24.** Schematic representation for the geometrical relationships between both shear and peel deformations  
 2 of the adhesive layer and the relative displacement of the surrounding adherends.  $\gamma$ : adhesive shear strain.  $\epsilon$ :  
 3 Adhesive peel strain.  $\gamma e$ : adhesive shear displacement jump between P2-P1.  $(1+\epsilon)e$ : adhesive peel displacement  
 4 jump between P2-P1.

6 **4.2.2. Test results and modelling under pure modes**

7 The constitutive traction separation law of the adhesive layer obtained in the case of pure mode I and pure mode  
 8 II loadings is presented in **Figure 25-(a)** and **Figure 26-(a)** respectively. The CZM parameters for pure mode I  
 9 and pure mode II are then provided in **Table 6** and **Table 7** respectively. On each pure mode, the model  
 10 obtained is composed by 3 parts: an elastic part, a plastic part and a softening part. The identification of CZM  
 11 parameters is performed on the envelope curves built from the cyclic response, using the elastic stiffness of  
 12 adherends. The hypothesis underlying is that the Young's modulus does not vary significantly during the plastic  
 13 phase. Even if this hypothesis does not hold at large strain of adherends, it allows drastic simplification of the  
 14 identification process. It means that the adherend stiffnesses used for the identification in **Eqs. (18), (21), (23)**  
 15 and **(24)** correspond to the initial elastic values. A numerical test is then performed assuming a nonlinear  
 16 behavior for both the adherends (following the trilinear approximation in **Table 4**, see **Appendix C**) and the  
 17 adhesive layer. The numerical test predictions, in terms of load / displacement curve, are then compared to the  
 18 experimental test results on DCB and ENF specimens in **Figure 25-(b)** and **Figure 26-(b)** respectively. A good  
 19 agreement is shown.

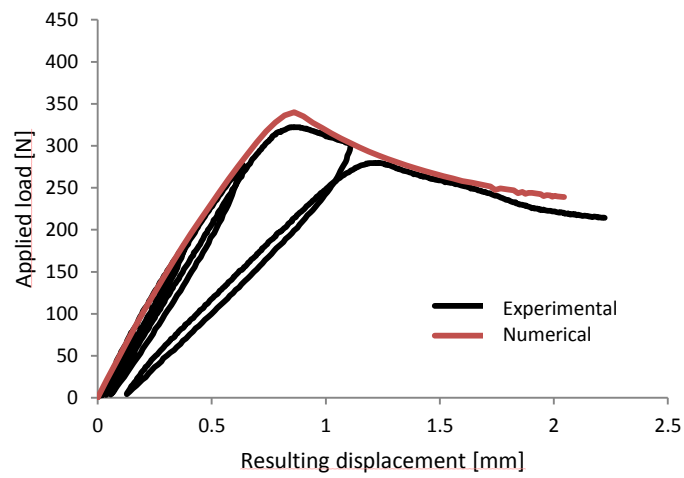


	a	L	t	e	b
Dimensions	30.69mm	70.0mm	3.96mm	0.180mm	22.0mm



(a)

1

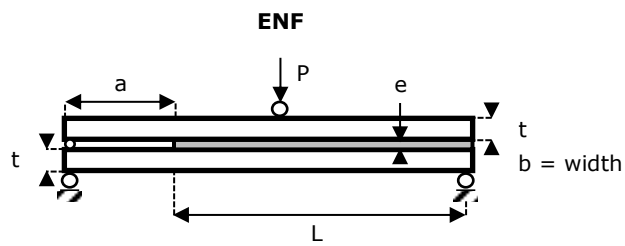


(b)

2

3 **Figure 25.** (a) Experimental adhesive traction separation law in pure mode I. (b) Comparison between

4 experimental results and numerical predictions in terms of load versus displacement curves.



5

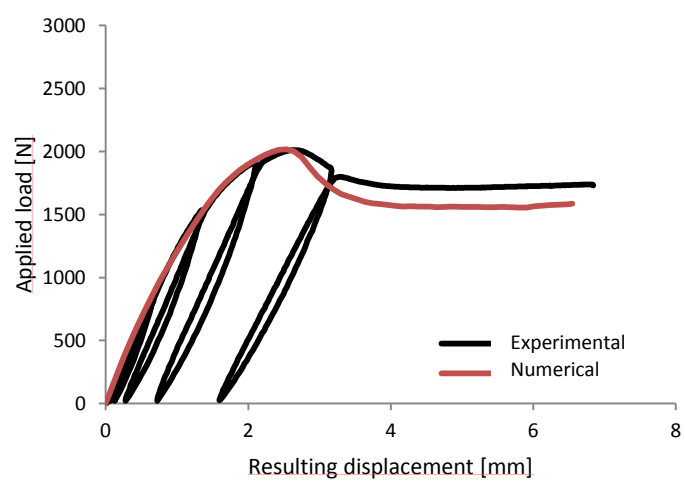
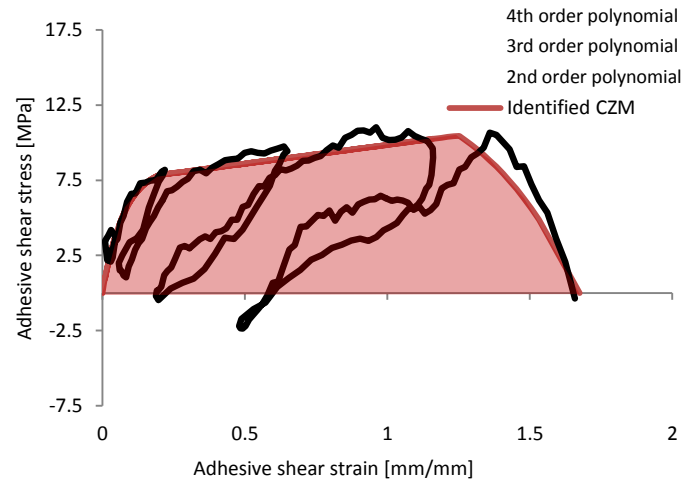
	a	L	t	e	b
Dimensions	29.82mm	71.34mm	3.96mm	0.230mm	22.0mm

6

7

— Experimental

(a)



1

2

3 **Figure 26.** (a) Experimental adhesive traction separation law in pure mode II. (b) Comparison between  
 4 experimental results and numerical predictions in terms of load versus displacement curves.

5

6

**Table 6.** CZM properties in pure mode I.

	Elastic	Plastic	Softening
Model (CZM)	$S(\varepsilon) = \frac{k_s \varepsilon_1}{\ln(e_s)} \left( 1 - \exp\left(\frac{\ln(e_s)}{\varepsilon_1} \varepsilon\right) \right)$	$S(\varepsilon) = S_1 + k_{s,1}(\varepsilon - \varepsilon_1)$	$S(\varepsilon) = S_2 \frac{\varepsilon_3 - \varepsilon}{\varepsilon_3 - \varepsilon_2}$
Parameters	$k_s = 250MPa$ $e_s = 0.030$ $\varepsilon_1 = 0.15$	$k_{s,1} = 2.5MPa$ $S_1 = 10.37MPa$ $\varepsilon_1 = 0.15$	$S_2 = 10.99MPa$ $\varepsilon_2 = 0.4$ $\varepsilon_3 = 0.75$
Validity	$0 \leq \varepsilon \leq \varepsilon_1$	$\varepsilon_1 \leq \varepsilon \leq \varepsilon_2$	$\varepsilon_2 \leq \varepsilon \leq \varepsilon_3$

7

8

**Table 7.** CZM properties in pure mode II

	Elastic	Plastic	Softening
Model (CZM)	$T(\gamma) = \frac{k_T \gamma_1}{\ln(e_T)} \left( 1 - \exp\left(\frac{\ln(e_T)}{\gamma_1} \gamma\right) \right)$	$T(\gamma) = T_1 + k_{T,1}(\gamma - \gamma_1)$	$T(\gamma) = T_2 \frac{\gamma_3^3 - \gamma^3}{\gamma_3^3 - \gamma_2^3}$

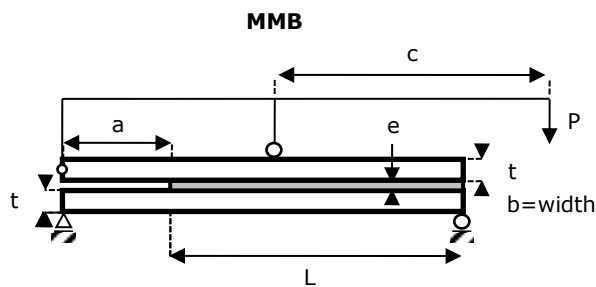
Parameters	$k_T = 110MPa$ $e_T = 0.075$ $\gamma_1 = 0.2$	$k_{T,1} = 2.5MPa$ $T_1 = 7.85MPa$ $\gamma_1 = 0.2$	$T_2 = 10.48MPa$ $\gamma_2 = 1.25$ $\gamma_3 = 1.675$
Validity	$0 \leq \gamma \leq \gamma_1$	$\gamma_1 \leq \gamma \leq \gamma_2$	$\gamma_2 \leq \gamma \leq \gamma_3$

1

2 4.2.3. Test results and modelling under mixed-mode I/II

3 As previously, the constitutive relationships of the adhesive layer when facing mixed-mode I/II solicitations are  
4 investigated using the direct method. Nevertheless, the exploitation of test results fails, due to the limited axial  
5 displacements of both upper and lower adherends nearby the adhesive crack tip. It results in badly conditioned  
6 measures of the adherends axial displacements, from which the differentiation with respect to  $x$  is insufficiently  
7 accurate. An alternative characterization method is then developed for determining the effective mixed-mode I/II  
8 properties of the tested MMB specimens. It is suggested to use an inverse characterization method based on  
9 numerical tests. The CZM properties in pure mode I and pure mode II are considered as well as the nonlinear  
10 adhered behavior. Both initiation and propagation mixed-mode criteria are assumed as following power law  
11 energetical relationships (see Eq. (7)). The idea is then to adjust the value of the value of the exponent  $n=m$  in  
12 order numerical prediction fit the experimental tests. In this study, the identification was made according to tests  
13 with two different value of mixed-mode ratio, by the use of two different lever arm denoted  $c$ . Similarly to the  
14 previous pure mode tests, the experimental test results and numerical test predictions for both mixed-mode ratios  
15 are compared in terms of load / displacement curve in Figure 27. The presented comparison is for  $n=m=1$ . Good  
16 agreement is shown.

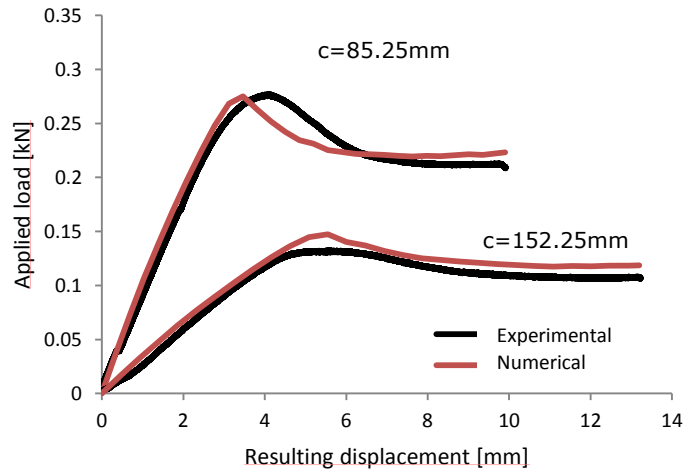
17



18

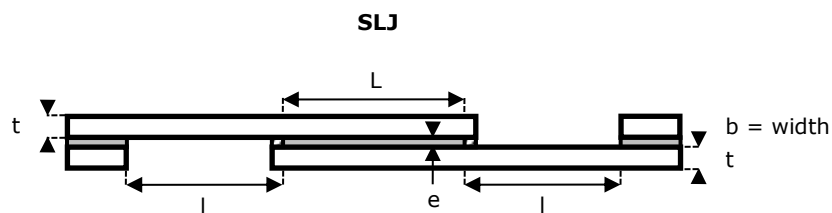
	a	L	t	e	b
Dimensions	30.21mm	70.89mm	3.96mm	0.180mm	22.0mm

19



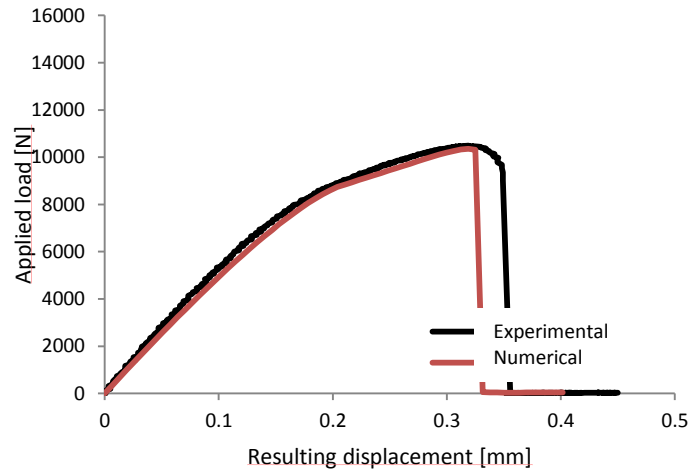
1  
 2 **Figure 27.** Determination of the effective mixed-mode properties of the adhesive layer using the inverse  
 3 method. Comparison between experimental results and semi-analytical predictions in terms of load versus  
 4 displacement curve.

5  
 6 In order to assess the relevance of the measured constitutive stress-strain relationships of the adhesive layer  
 7 subjected to pure mode I, pure mode II and mixed-mode I/II adhesive loadings, experimental test results and  
 8 numerical test predictions are compared on the configuration of the SLJ configuration. As shown, in **Figure 28**,  
 9 good agreement is shown in terms of both stiffness and maximum load bearing capability of the SLJ joint  
 10 specimen. Nevertheless, the single-lap joint configuration is known to be submitted significantly more in mode I  
 11 than in mode II due to the eccentricity of the load path generating secondary bending moment and large peel  
 12 stresses at both overlap ends. To validate the behavior law under mixed-mode, other experimental tests should be  
 13 conducted based on various loading and geometrical configurations.



	L	l	t	e	b
Dimensions	51.4mm	29.35mm	3.96mm	0.120mm	22.0mm

14  
 15



1  
 2 **Figure 28.** Comparison between experimental results and semi analytical predictions in terms of load versus  
 3 displacement curve.

4  
 5 **5. Conclusion**

6 In this paper, a direct method for the assessment of the CZM parameters of a thin adhesive layer is presented and  
 7 then implemented. This method is based on the measurement of the displacement field of adherends at the crack  
 8 tip of classical adhesively bonded specimens (i.e.: ENF, DCB, MMB), allowing for pure mode I, pure mode II  
 9 and mixed-mode I/II loadings. Nevertheless, the identification presented remains dependent of the modelling  
 10 framework. The experimental implementation makes use of a methacrylate-based two-component adhesive  
 11 paste, found under the commercial reference SAF30 MIB manufactured by AEC Polymers / Bostik (ARKEMA  
 12 Group). The adherends are made in aluminum alloy (6060 series). The adhesive constitutive stress-strain  
 13 relationships are derived from the monitoring of the evolution at crack tip of both the relative displacement of  
 14 interfaces and the displacement field of the adherend, using the DIC technique. The main difficulty encountered  
 15 within the experimental implementation concerns the experimental measurements. Indeed, a dedicated data  
 16 preprocessing (see [Appendix B](#)) is developed to best fit the experimental data coming from the DIC technique.  
 17 The use of experimental measurement providing a higher resolution such as Speckle interferometry could be  
 18 more suitable.

19 In pure mode I and pure mode II, it is shown that the adhesive layer experiences three distinct phases. The first  
 20 one, the linear elastic phase, appears as extremely limited compared to the whole deforming capability of the  
 21 adhesive layer. A mathematical model is then provided for each mode. Under mixed-mode, the data  
 22 preprocessing fails in interpreting the experimental measurements, so that a dedicated method is suggested. The  
 23 mathematical models are then implemented to perform numerical tests using a simplified stress analysis based on

1 ME. In terms of global behavior, the predictions of numerical tests are in a close agreement with the results of  
2 experimental tests, up to the final failure of specimens. Besides, it is indicated that the identification of CZM  
3 properties presented in this paper involves specimens, the adherends of which experienced plasticization. Even if  
4 the simplified stress analysis based on ME allowing for numerical tests supports both nonlinear adhesive and  
5 adherend material behavior, the embedded level of complexity in the experimental test procedure appears as  
6 elevated. The implementation of the direct method should be then tested through various combinations of  
7 adherends and adhesive materials and various geometries, some of which should prevent the adherends to  
8 plasticize, to assess the reliability of the experimental procedure. The effect of the adhesive thickness on the  
9 material law could be investigated using measurement means with a better performance.

10

### 11 **Acknowledgement**

12 The authors gratefully acknowledge Mr Christian Bret, CEO of AEC Polymers, for the supplying of materials.

13

### 14 **Appendix A**

15 Considering the local equilibrium equations Eqs. (8), the adhesive stresses are replaced by their expressions as  
16 functions of adherend displacements Eqs. (9). In conjunction Eqs (10), it results in a system of twelve linear  
17 first-order ordinary differential:

$$\left\{ \begin{array}{l}
 \frac{du_1}{dx} = \frac{D_1}{\Delta_1} N_1 + \frac{B_1}{\Delta_1} M_1 \\
 \frac{du_2}{dx} = \frac{D_2}{\Delta_2} N_1 + \frac{B_2}{\Delta_2} M_2 \\
 \frac{dv_1}{dx} = \theta_1 \\
 \frac{dv_2}{dx} = \theta_2 \\
 \frac{d\theta_1}{dx} = \frac{B_1}{\Delta_1} N_1 + \frac{A_1}{\Delta_1} M_1 \\
 \frac{d\theta_2}{dx} = \frac{B_2}{\Delta_2} N_2 + \frac{A_2}{\Delta_2} M_2 \\
 \frac{dN_1}{dx} = bk_{II}u_1 + bk_{II}h_1\theta_1 - bk_{II}u_2 + bk_{II}h_2\theta_2 \\
 \frac{dN_2}{dx} = -bk_{II}u_1 - bk_{II}h_1\theta_1 + bk_{II}u_2 - bk_{II}h_2\theta_2 \\
 \frac{dv_1}{dx} = bk_Iv_1 - bk_Iv_2 \\
 \frac{dv_2}{dx} = -bk_Iv_1 + bk_Iv_2 \\
 \frac{dM_1}{dx} = bh_1k_{II}u_1 + bk_{II}h_1h_1\theta_1 - bh_1k_{II}u_2 + bk_{II}h_1h_2\theta_2 - V_1 \\
 \frac{dM_2}{dx} = bh_2k_{II}u_1 + bk_{II}h_2h_2\theta_1 - bh_2k_{II}u_2 + bk_{II}h_2h_2\theta_2 - V_2
 \end{array} \right. \quad (A1)$$

19 This system can be written as  $\frac{dX}{dx} = AX$  where  $A$  is 12x12 matrix with real constant components and the  
20 unknown vector  $X$  such that  $X=(u_1 \ u_2 \ v_1 \ v_2 \ \theta_1 \ \theta_2 \ N_1 \ N_2 \ V_1 \ V_2 \ M_1 \ M_2)$ . But the elementary stiffness matrix

1 corresponds to the relationship between the vector of nodal forces and the vector of nodal displacements  
 2 (Paoissien 2006a, Paoissien 2006b, Paoissien *et al.* 2007, Paoissien *et al.* 2013, Lélías *et al.* 2015), such as:

$$\begin{pmatrix} -N_1(0) \\ -N_2(0) \\ N_1(\Delta) \\ N_2(\Delta) \\ -V_1(0) \\ -V_2(0) \\ V_1(\Delta) \\ V_2(\Delta) \\ -M_1(0) \\ -M_2(0) \\ M_1(\Delta) \\ M_2(\Delta) \end{pmatrix} = K_{BBE} \begin{pmatrix} u_1(0) \\ u_2(0) \\ u_1(\Delta) \\ u_2(\Delta) \\ v_1(0) \\ v_2(0) \\ v_1(\Delta) \\ v_2(\Delta) \\ \theta_1(0) \\ \theta_2(0) \\ \theta_1(\Delta) \\ \theta_2(\Delta) \end{pmatrix} \quad (A2)$$

3  
 4  
 5 The fundamental matrix of  $A$ , termed  $\Phi_A$ , is computed at  $x=0$  and  $x=\Delta$ ; using the SCILAB software, the  
 6 associated command is “expm”:

$$\begin{cases} \Phi_A(x=0) = \text{expm}(A, 0) \\ \Phi_A(x=\Delta) = \text{expm}(A, \Delta) \end{cases} \quad (A3)$$

7  
 8 From these both 12\*12 matrices, two matrices  $M'$  and  $N'$  are extracted.  $M'$  ( $N'$ ) is composed of the lines related  
 9 to the nodal displacements (forces). For each, a first block of six lines and twelve rows comes from  $\Phi_A(x=0)$  and  
 10 the second block of six lines and twelve rows come from  $\Phi_A(x=\Delta)$ , such that:

$$\begin{cases} M' = \Phi_U(0, \Delta) = \begin{pmatrix} [\Phi_A(x=0)]_{i=1,2,3,4,5,6; j=1:12} \\ [\Phi_A(x=\Delta)]_{i=1,2,3,4,5,6; j=1:12} \end{pmatrix} \\ N' = \Phi_F(0, \Delta) = \begin{pmatrix} [\Phi_A(x=0)]_{i=7,8,9,10,11,12; j=1:12} \\ [\Phi_A(x=\Delta)]_{i=7,8,9,10,11,12; j=1:12} \end{pmatrix} \end{cases} \quad (A4)$$

11  
 12 where  $i$  ( $j$ ) indicates the line (row) number.

13 As  $K_{BBE}$  is defined according to  $([u_1(0) u_2(0) u_1(\Delta) u_2(\Delta) v_1(0) v_2(0) v_1(\Delta) v_2(\Delta) \theta_1(0) \theta_2(0) \theta_1(\Delta) \theta_2(\Delta)])$ , a  
 14 simple rearrangement of the order of lines of  $M'$  is performed to produce the matrix  $M$ . Similarly, the matrix  $N'$   
 15 is submitted to the same operation. In a same way, the terms related to nodal forces at  $x=0$  are multiplied by  $-I$  to  
 16 follow the arrangement  $([-N_1(0) -N_2(0) N_1(\Delta) N_2(\Delta) -V_1(0) -V_2(0) V_1(\Delta) V_2(\Delta) -M_1(0) -M_2(0) M_1(\Delta) M_2(\Delta)])$ . It  
 17 leads to the definition of the matrix  $N$ . The elementary stiffness matrix  $K_{BBE}$  is equal to the product of  $N$  and the  
 18 inverse of  $M$  (Paoissien *et al.* 2013, Lélías *et al.* 2015):  $K_{BBE} = N.M^{-1}$ .

19 Even if it is not the topic of this paper, it is obvious that this previous approach can be easily used to develop  
 20 ME, under different local equilibrium equations (e.g. Hart-Smith (Hart-Smith 1973, Luo and Tong 2009,  
 21 Paoissien *et al.* 2018) or under different constitutive equations (e.g. Tsai *et al.* (Tsai *et al.* 1998)) and/or  
 22 including different number layers of adhesives and adherends (e.g. double lap joint configuration). It is indicated  
 23 that the resolution using the exponential matrix was already been used in previous works (Gustafson *et al.* 2006),

1 (Gustafson and Waas 2007, Gustafson 2008, Gustafson and Waas 2009, Stapleton and Waas 2009, Stapleton *et*  
2 *al.* 2010, Stapleton 2012, Stapleton *et al.* 201, Stapleton *et al.* 2017). The use of the resolution scheme using the  
3 exponential matrix is suitable in the case of nonlinear analysis since a mesh is required. It is suitable in the case  
4 of non-homogeneous elastic adhesive properties too (Paoissien *et al.* 2018). Besides, it is useful for the  
5 formulation of new macro-elements under various simplified hypotheses (Paoissien *et al.* 2018).

## 6 7 **Appendix B**

8 The data pre-processing algorithm used to reduce experimental noises from the measured adherend-to-adherend  
9 displacement fields then lies on the digital mapping of the adherend-to-adherend axial (transverse) displacement  
10 fields as a set of 2D matrices. First, the evolution of the axial (transverse) displacement field of each adherend is  
11 mapped as 3D tensors resuming both the distributions of the adherend axial (transverse) displacements nearby  
12 the adhesive crack tip as well as their respective evolutions. Then, the constructed 3D tensors of dimensions  $x$ ,  $y$   
13 and  $t$  are rearranged in the form of simpler 2D matrices so that their new dimensions are respectively  $y$  and  $x*t$   
14 (see Figure B-1). The constructed 2D matrices are then filtered using the rank- $R$  reduction approximation based  
15 on the SVD of the raw experimental results, so that  $R$  is chosen to capture 95% of the original data energy in the  
16 sense of the Frobenius norm (see Figure B-2). The evolution of each adherend axial and transverse displacement  
17 fields are then reconstructed from their respective decompositions and rearranged in the form of 3D tensors, so  
18 that the displacements of the upper (lower) neutral fiber are finally extracted from the reconstructed axial and  
19 transverse displacement fields and formatted into the relevant beam or plate theory (see Figure B-3). Finally, the  
20 differentiation of the adherends cross-section rotation is ensured by fitting a polynomial series so that the vertical  
21 deviation with experimental data is minimized in the sense of the least squares method by using the Moore-  
22 Penrose pseudo inverse technique.

23 Besides, a full factorial design of experiments is performed in order to assess the algorithmic parameters on the  
24 accuracy of the measure. It consists in the following: (i) vary one factor at a time, (ii) perform experiments for all  
25 levels and combination of levels for all factors, (iii) hence perform a large number of experiments, (iv) so that all  
26 effects and interactions are captured. The main results for each of five factors selected are presented hereafter.

27 (i) The initial signal to noise ratio appears as a key parameter in increasing the accuracy of measuring the  
28 successive derivatives of the upper adherend displacement field. It suggests that a significant attention has to be  
29 given into reducing the noise of the measured signal before any pre-processing of the data. This can be achieved  
30 in various ways so that it results in improving the overall quality of the displacement measures (DIC).

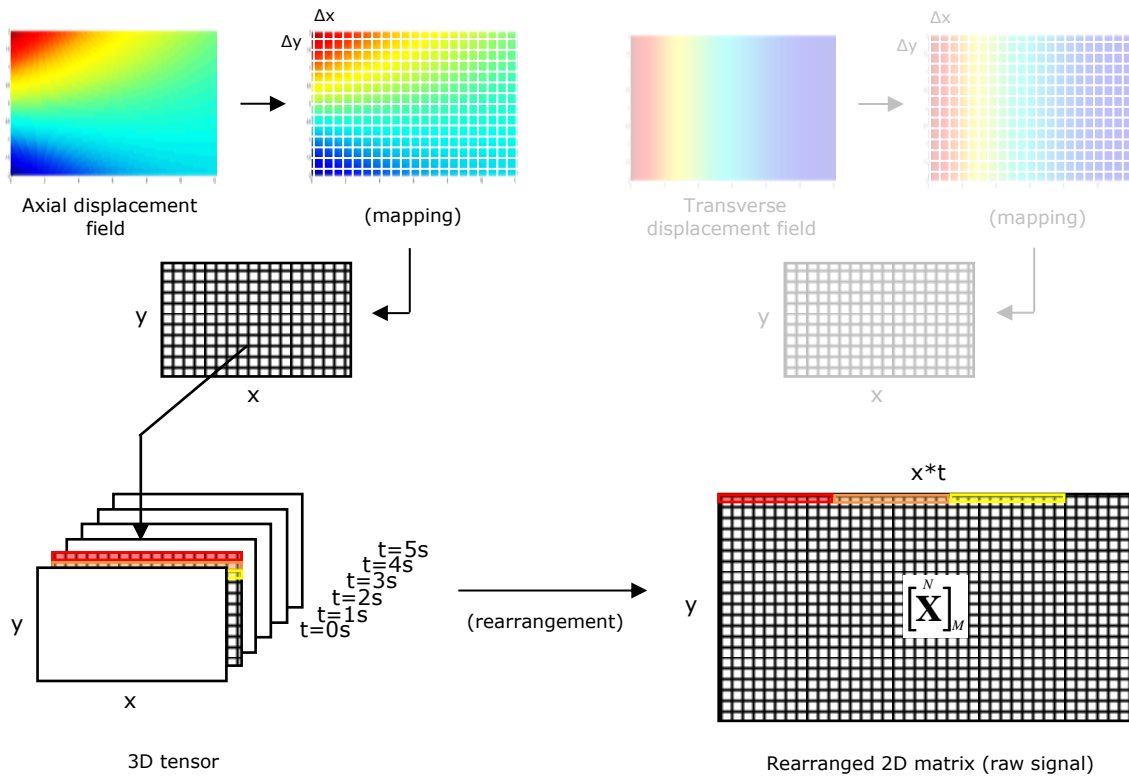
1 (ii) The spatial resolution of the instantaneous images of the upper adherend displacement field also appears as a  
2 key parameter in increasing the accuracy of the estimation of the successive derivatives of the upper adherend  
3 displacements. A particular attention has then to be given to measuring the displacements of the upper adherend  
4 with a sufficient enough spatial resolution.

5 (iii) On another side, the time resolution (i.e. number of images of the upper adherend displacement field taken  
6 during the experiment) appears as negligibly influencing the accuracy of the estimation of the successive  
7 derivatives of the upper adherend displacements. Its own effect as well as its respective interactions with other  
8 factors can be legitimately neglected at first sight.

9 (iv) Similarly to the initial signal to noise ratio or the spatial resolution of the displacement images, the degree of  
10 the polynomial series used for fitting/differentiating the pre-processed displacements also appears as a parameter  
11 that has to be chosen with extreme caution. Indeed, although increasing the degree of the polynomial series from  
12 four to six appears as negligibly influencing the overall accuracy of the measure, increasing it from six to eight  
13 results in a serious degradation of the accuracy of the measure. This degradation of the accuracy of the  
14 measurement using high order polynomials is a well-known issue, and is due to the oscillation of the polynomial  
15 series around the experimental set of data points for increasing degrees. A particular attention has then to be  
16 given in choosing the best compromise between fitting the experimental points using high order polynomials  
17 functions and preserving the overall accuracy of the measurement of its successive derivatives.

18 (v) Finally, the choice of the Moore-Penrose pseudo inverse model for minimizing in the sense of the least  
19 squares method the vertical deviation between the polynomial function (i.e. used for fitting/differentiating the set  
20 of experimental data points) and the experimental data points themselves appears as a worthwhile way of  
21 influencing the accuracy of the measured displacement derivatives. It is then suggested that simultaneously  
22 accounting for both  $v(x)$  and  $\theta(x)=dv(x)/dx$  when fitting/differentiating the experimental set of data points  
23 significantly increases the accuracy of the measurement.

24

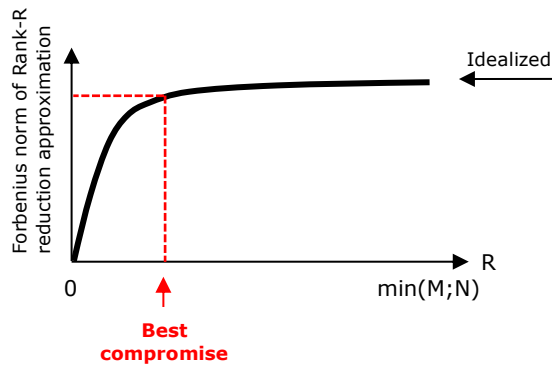
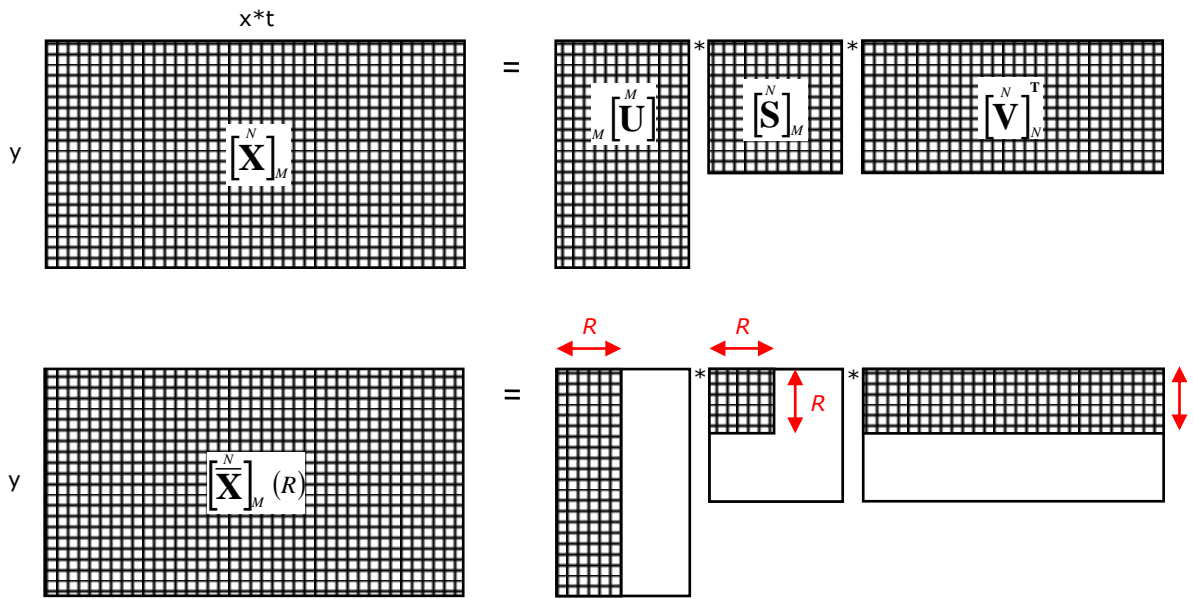


1

2

Figure B-1. Digital mapping of the adherend-to-adherend axial and transverse displacement fields.

3



1  
2  
3  
4

Figure B-2. Filtering of the experimental results using the rank- $R$  reduction approximation based on Singular Value Decomposition (SVD).

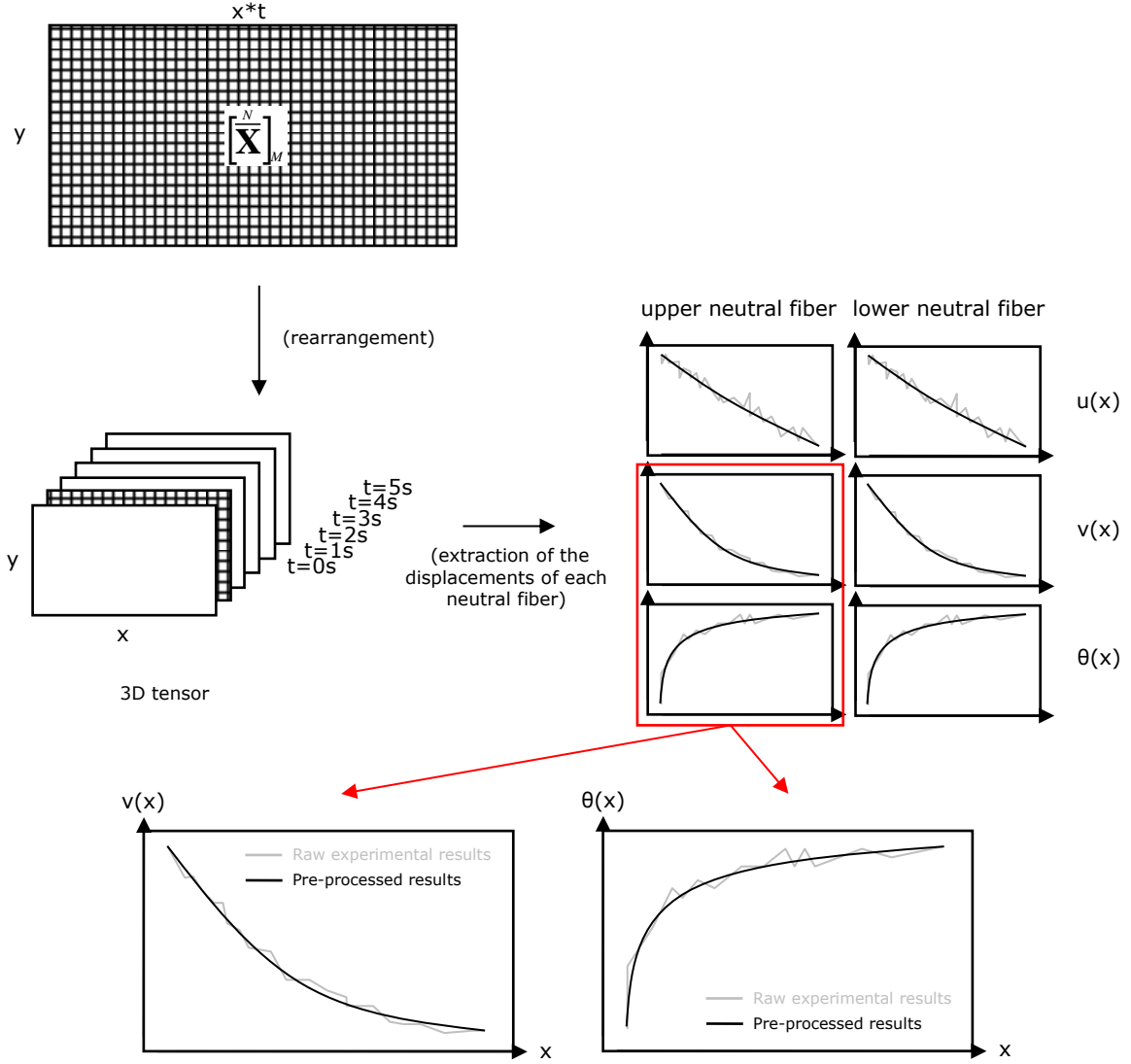


Figure B-3. Extraction of the displacements of each adherend neutral fiber.

1  
2

3

#### 4 Appendix C

5 The beam model use for the adherends allows for the consideration of the Young's modulus graduation in the  
6 thickness. The constitutive equations for the normal force and bending moment are derived as it follows.

7 Using the Euler-Bernoulli kinematics, the normal force  $N_j$  of the adherend  $j$  is written such as:

$$8 \quad N_j = \int \sigma_{xx} dS = \int E_j(y) \epsilon_{xx} dS = \int E_j(y) \left[ \frac{du_j}{dx} - y \frac{d\theta_j}{dx} \right] dS \quad (C-1)$$

9 It leads to:

$$10 \quad N_j = \left( \int E_j(y) dS \right) \frac{du_j}{dx} - \left( \int E_j(y) y dS \right) \frac{d\theta_j}{dx} = A_j \frac{du_j}{dx} - B_j \frac{d\theta_j}{dx} \quad (C-2)$$

11 The same approach is used for the bending moment:

$$12 \quad M_j = \int -y \sigma_{xx} dS = \int -y E_j(y) \epsilon_{xx} dS = \int -y E_j(y) \left[ \frac{du_j}{dx} - y \frac{d\theta_j}{dx} \right] dS \quad (C-3)$$

1 leading to:

$$2 \quad \mathbf{M}_j = -\left(\int \mathbf{E}_j(\mathbf{y})\mathbf{y}d\mathbf{S}\right)\frac{du_j}{dx} + \left(\int \mathbf{E}_j(\mathbf{y})\mathbf{y}^2 d\mathbf{S}\right)\frac{d\theta_j}{dx} = -\mathbf{B}_j\frac{du_j}{dx} + \mathbf{D}_j\frac{d\theta_j}{dx} \quad (\text{C-4})$$

3 To take into account for the nonlinear behavior of adherends, the iterative Newton-Raphson procedure associated  
4 with the secant stiffness matrix is used, which is detailed in (Lélias 2015). The secant Young's modulus of  
5 adherends is then updated following the behavior law identified in Table 4. As a result the stiffness parameters  
6  $A_j$ ,  $B_j$  and  $D_j$  are updated consequently. In particular, when the isotropic adherends begin to plasticize, the  
7 coupling membrane-bending stiffness  $B_j$  could become different from zero.

8

## 9 REFERENCES

10 (Alfredsson *et al.* 2003) Alfredsson K.S., Biel A. and Leffler K., 2003. An experimental method to determine the  
11 complete stress-deformation relation for a structural adhesive layer loaded in shear. In: Proceeding to 9<sup>th</sup>  
12 International Conference on The Mechanical Behavior of Materials, Geneva, Switzerland.

13

14 (Alfredsson 2004) Alfredsson K.S., 2004. On the instantaneous energy release rate of the end notched flexure  
15 adhesive joint specimen. *Int. J. Solids Struct.* 41, 4787-4807.

16

17 (Allix and Ladevèze 1996) Allix O. and Ladevèze P., 1996. Damage mechanics of interfacial media: Basic  
18 aspects, identification and application to delamination, in *Damage and Interfacial Debonding in Composites*,  
19 *Studies in Applied Mechanics*, 44, D. Allen and G. Voyiadjis (Eds.), pp. 167-88, Elsevier.

20

21 (Andersson and Stigh 2004) Anderson T. and Stigh U., 2004. The stress-elongation relation for an adhesive  
22 loaded in peel using equilibrium of energetic forces. *Int. J. Solids Struct.* 41, 413-434.

23

24 (Andrews and Patterson 1973) Andrews H.C. and Patterson C.L., 1976. Singular value decomposition and digital  
25 image processing. *IEEE Transactions on ASSP-24*, 26-53

26

27 (Azari *et al.* 2009) Azari S., Eskandarian M., Papini M., Schroeder J.A. and Spelt J.K., 2009. Fracture load  
28 predictions and measurements for toughened epoxy adhesive joints. *Eng. Fract. Mech.* 76, 2039-2055.

29

1 (Bartczak and Geleski 2010) Bartczak Z. and Geleski A., 2010. Plasticity of semicrystalline polymers.  
2 Macromolecular Symposia 294, Issue 1, 67-90.  
3  
4 (Camphilho *et al.* 2013) Campilho R.D.S.G., Banea M.D., Neto J.A.B.P. and Da Silva L.F.M., 2013. Modelling  
5 adhesive joints with cohesive zone models: Effects of the cohesive law shape of the adhesive layer. *Int. J. Adhes.*  
6 *Adhes.* 44, 48-56.  
7  
8 (Clarke *et al.* 2003) Clarke J.L., 2003. Structural design of polymer composites: Eurocomp design code and  
9 background document. CRCpress. ISBN 0203475135, 9780203475133.  
10  
11 (Cui *et al.* 2014) Cui H., Koussios S., Li Y. and Beukers A., 2014. Constitutive law of adhesive layer measured  
12 with mixed-mode bending test. *Eng. Fract. Mech.* 127, 235-251.  
13  
14 (Da Silva and Campilho 2012) Da Silva L.F.M. and Campilho R.D.S.G., 2012. Advances in numerical modeling  
15 of adhesive joints. *Springer Briefs in Computational Mechanics*, DOI 10.1007/978-642-23608\_1.  
16  
17 (De Moura *et al.* 2009) De Moura M.F.S.F., Campilho R.D.S.G. and Goncalves J.P.M., 2009. Mixed-mode  
18 cohesive damage model applied to the simulation of the mechanical behavior of laminated composite adhesive  
19 joints. *J. Adhes. Sci. Technol.* 23, Issue 10-11, 1477-1491.  
20  
21 (Fraisse and Schmit 1993) Fraisse P. and Schmit F., 1993. Use of J-integral as fracture parameter in simplified  
22 analysis of bonded joints. *Int. J. Fract.* 63, 59-73.  
23  
24 (Goland and Reissner 1944) Goland M. and Reissner E., 1944. The stresses in cemented joints, *J. Appl. Mech.*  
25 11, A17-A27.  
26  
27 (Gowrishankar S. *et al.* 2012) Gowrishankar S., Mei H., Liechti K.M. and Huang R., 2012. A comparison of  
28 direct and iterative methods for determining traction-separation relations. *Int. J. Fract.* 177, 109-128.  
29

1 [\(Goustianos and Sørensen 2012\)](#) Goustianos S. and Sørensen B.F., 2012. Path dependence of truss-like mixed  
2 mode cohesive laws. *Eng. Fract. Mech.* 91, 117-132.  
3  
4 [\(Gustafson \*et al.\* 2006\)](#) Gustafson, P.A., Bizard, A., M. Waas., 2006. A macroscopic joint finite element for a  
5 symmetric double lap joint. *Proceedings of the American Society of Composites 21<sup>st</sup> Annual Technical*  
6 *Conferences*, No. 24, American Society of Composites.  
7  
8 [\(Gustafson and Waas 2007\)](#) Gustafson, P.A., Waas, A.M., 2007. A macroscopic finite element for a symmetric  
9 double lap joint subjected to mechanical and thermal loading. 48th AIAA/ASME/ASCE/AHS/ASC Structures,  
10 Structural Dynamics, and Materials Conference, 23-26 April 2007, Honolulu, Hawaii.  
11  
12 [\(Gustafson 2008\)](#) Gustafson, P.A., 2018. Analytical and experimental methods for adhesively bonded joints  
13 subjected to high temperatures PhD thesis, University of Michigan. Michigan.  
14  
15 [\(Gustafson and Waas 2009\)](#) Gustafson, P.A., Waas, A.M., 2009. A bonded joint finite element for a symmetric  
16 double lap joint subjected to mechanical and thermal loads. *Int. J. Numer. Meth. Eng.*, 79(1), 94-126.  
17  
18 [\(Hart-Smith 1973\)](#) Hart-Smith L.J., 1973. Adhesive bonded single lap joints. NASA Technical Report, CR-  
19 112236, Douglas Aircraft Company, Long Beach, California.  
20  
21 [\(Hart-Smith 1980\)](#) Hart-Smith L.J., 1980. Adhesive Bonding of Aircraft Primary Structures. SAE Technical  
22 Paper 801209.  
23  
24 [\(Högberg 2006\)](#) Högberg J.L., 2006. Mixed-mode testing of adhesive layer. In: *Proceeding to 27th International*  
25 *Symposium on Materials Science, Polymer Composite Materials for Wind Power Turbines*, Risø, Denmark.  
26  
27 [\(Högberg and Stigh 2006\)](#) Högberg J.L. and Stigh U., 2006. Specimen proposals for mixed-mode testing of  
28 adhesive layer. *Eng. Fract. Mech.* 73, 2541-2556.  
29

1 (Jumel *et al.* 2006) Jumel J., Budzik M.K., Ben Salem N., Shanahan M.E.R., 2013. Instrumented end notched  
2 flexure – Crack propagation and process zone monitoring. Part I: Modelling and Analysis. *Int. J. Adhes. Adhes.*  
3 50, N°2, 297-309.  
4  
5 (Khoramishad *et al.* 2010) Khoramishad H., Crocombe A.D., Katnam K.B. and Ashcroft I.A., 2010. A  
6 generalized damage model for constant amplitude fatigue loading of adhesively bonded joints. *Int. J. Adhes.*  
7 *Adhes.* 30, 513-521.  
8  
9 (Khoramishad *et al.* 2011) Khoramishad H., Crocombe A.D., Katnam K.B. and Ashcroft I.A., 2011. Fatigue  
10 damage modeling of adhesively bonded joints under variable amplitude loading using cohesive zone model. *Eng.*  
11 *Fract. Mech.* 78, 3212-3225.  
12  
13 (Kelly 2006) Kelly G., 2006. Quasi-static strength and fatigue life of hybrid (bonded/bolted) composite single-  
14 lap joints. *J. Compos. Struct.* 72, 119-129.  
15  
16 (Kenane and Benzeggagh 1997) Kenane M. and Benzeggagh M.L., 1997. Mixed-mode delamination fracture  
17 toughness of unidirectional glass/epoxy composites under fatigue loading. *Compos. Sci. Technol.* 57, 597-605.  
18  
19 (Leffler *et al.* 2007) Leffler K., Alfredsson K.S. and Stigh U., 2007. Shear behavior of adhesive layers. *Int. J.*  
20 *Solids Struct.* 44, 530-545.  
21  
22 (Lélias *et al.* 2015) Lélias G., Paroissien E., Lachaud F., Morlier J., Schwartz S. and Gavaille C., 2015. An  
23 extended semi-analytical formulation for fast and reliable mode I/II stress analysis of adhesively bonded joints.  
24 *Int. J. Solids and Struct.* 62, 18-38.  
25  
26 (Luo and Tong 2009) Luo Q. and Tong L., 2009. Analytical solutions for nonlinear analysis of composite single-  
27 lap joints, *Int. J. Adhes. Adhes.* 29, 144-154.  
28

1 (Paoissien 2006a) Paoissien E., 2006. Contribution aux Assemblages Hybrides (Boulonnés/Collés) –  
2 Application aux Jonctions Aéronautiques. PhD Dissertation (in French), Université de Toulouse III (2006), on  
3 line <http://thesesups.ups-tlse.fr/3/>  
4  
5 (Paoissien et al. 2006b) Paoissien E., Sartor M., Huet J. and Lachaud F., 2006. Hybrid (Bolted/Bonded) Joints  
6 Applied to Aeronautic Parts: Analytical Two-Dimensional Model of a Hybrid (Bolted/Bonded) Single-Lap Joint.  
7 47th AIAA/ASME/ASCE/AHS/ASC Structures, Structural Dynamics, and Material Conference (47th SDM  
8 AIAA), 1-4 May 2006, Newport (RI), paper AIAA-2006-2268  
9  
10 (Paoissien et al. 2007) Paoissien E., Sartor M., Huet J. and Lachaud F., 2007. Analytical two-dimensional  
11 model of a hybrid (bolted/bonded) single-lap joint. *J. Aircraft* 44, 573-582.  
12  
13 (Paoissien et al. 2013) Paoissien E., Lachaud F. and Jacobs T., 2013. A simplified stress analysis of bonded  
14 joints using macro-elements. In: *Advances in Modeling and Design of Adhesively Bonded Bonded Systems*, S.  
15 Kumar and K.L. Mittal (Eds), 93-146, Wiley-Scrivener, Beverly, Massachusetts.  
16  
17 (Paoissien et al. 2018) Paoissien E. da Silva L.F.M., Lachaud F., 2018. Simplified stress analysis of  
18 functionally graded single-lap joints subjected to combined thermal and mechanical loads. *Compos. Struct.*, Vol.  
19 203, pp. 85-100 [DOI: 10.1016/j.compstruct.2018.07.015]  
20  
21 (Reeder and Crews 1990) Reeder J.R. and Crews J.R., 1990. Mixed-mode bending method for delamination  
22 testing. *AIAA J.* 28, N°7, 1270-1276.  
23  
24 (Rice 1968) Rice J.R., 1968. A path independent integral and the approximate analysis of strain concentration by  
25 notches and cracks. *J. of Appl. Mech.* 35, 379-386.  
26  
27 (Stapleton and Waas 2009) Stapleton, S.E., P.A., Waas, A.M., 2007. Macroscopic finite element for a single lap  
28 joint. 50th AIAA/ASME/ASCE/AHS/ASC Structures, Structural Dynamics, and Materials Conference, 4-7 May  
29 2009, Palm Springs, California.  
30

1 (Stapleton *et al.* 2010) Stapleton, S.E., P.A., Waas, A.M., Bednarczyk, B.A., 2010. Modelling progressive failure  
2 of bonded joints using a single joint finite element. 51st AIAA/ASME/ASCE/AHS/ASC Structures, Structural  
3 Dynamics, and Materials Conference, 12-15 April 2010, Orlando, Florida.  
4  
5 (Stapleton 2012) Stapleton, S.E., 2012. The analysis of adhesively bonded advanced composite joints using joint  
6 finite elements. PhD thesis, University of Michigan. Michigan.  
7  
8 (Stapleton *et al.* 2012) Stapleton, S.E., Waas A.M., Arnold, S.M., 2012. Functionally graded adhesive joints. *Int.*  
9 *J. Adhes. Adhes.*, 35, 36-49.  
10  
11 (Stapleton *et al.* 2017) Stapleton, S.E., Weimer, J., Spengler, J., 2017. Design of functionally graded joints using  
12 a polyurethane-based adhesive with varying amounts of acrylate, *Int. J. Adhes. Adhes.*, 76, 38-46.  
13  
14 (Tsai *et al.* 1998) Tsai M.Y., Oplinger D.W. and Morton J., 1998. Improved theoretical solutions for adhesive  
15 lap joints. *Int. J. Solids Struct.* 35, 1163-1185.  
16  
17 (Turon *et al.* 2010) Turon A., Camanho P.P., Costa J. and Renart J., 2010. Accurate simulation of delamination  
18 growth under mixed-mode loading using cohesive elements: Definition of interlaminar strengths and elastic  
19 stiffness. *Compos. Struct.* 92, 1857-1864.  
20  
21 (Valoroso and Champaney 2004) Valoroso N. and Champaney L., 2004. A damage model for simulating  
22 decohesion in adhesively bonded assemblies. In: *Proceeding to European Congress on Computational Methods*  
23 *in Applied Sciences and Engineering*, Jyväskylä, Finland.  
24  
25 (Weissgraeber *et al.* 2014) Weissgraeber P., Stein N. and Becker W., 2014. A general sandwich type model for  
26 adhesive joints with composite adherends. *Int. J. Adhes. Adhes.* 55, 56-63.  
27  
28 (Wu *et al.* 2016) Wu C., Gowrishankar S., Huang R. and Liechit K.M., 2013. On determining mixed-mode  
29 traction-separation relations for interfaces. *Int. J. Fract.* 202, 1-19.  
30